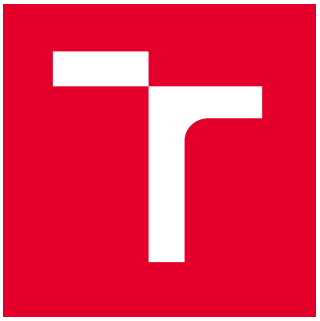



# BRNO UNIVERSITY OF TECHNOLOGY

VYSOKÉ UČENÍ TECHNICKÉ V BRNĚ

## FACULTY OF MECHANICAL ENGINEERING

FAKULTA STROJNÍHO INŽENÝRSTVÍ

## INSTITUTE OF SOLID MECHANICS, MECHATRONICS AND BIOMECHANICS

ÚSTAV MECHANIKY TĚLES, MECHATRONIKY A BIOMECHANIKY


# STRESS-STRAIN ANALYSIS OF THE AUTOMOBILE REAR AXLE UNDER IMPACT TO THE OBSTACLE

NAPĚŤOVĚ-DEFORMAČNÍ ANALÝZA ZADNÍ NÁPRAVY AUTOMOBILU PŘI NÁRAZU DO PŘEKÁŽKY

MASTER'S THESIS

DIPLOMOVÁ PRÁCE


AUTHOR — Bc. Ondrej Bodo

AUTOR PRÁCE

SUPERVISOR — doc. Ing. František Šebek, Ph.D.

VEDOUCÍ PRÁCE



BRNO 2026

BRNO UNIVERSITY OF TECHNOLOGY
FACULTY OF MECHANICAL ENGINEERING

# Master's Thesis Assignment

| | |
|---|---|
| Institute: | Institute of Solid Mechanics, Mechatronics and Biomechanics |
| Student: | **Bc. Ondrej Bodo** |
| Degree programm: | Engineering Mechanics and Biomechanics |
| Branch: | Engineering Mechanics |
| Supervisor: | **doc. Ing. František Šebek, Ph.D.** |
| Academic year: | 2025/26 |

As provided for by the Act No. 111/98 Coll. on higher education institutions and the BUT Study and Examination Regulations, the director of the Institute hereby assigns the following topic of Master's Thesis:

## Stress–strain analysis of the automobile rear axle under impact to the obstacle

**Brief Description:**

The impact of the twist–beam rear suspension on the obstacle can cause profile damage, leading to the initiation of the crack and its propagation. Therefore, it is necessary to have a knowledge of the conditions that threaten the integrity of the cross beam to avoid a subsequent crash, either immediately after the impact or after a subsequent use of the vehicle. The effective prediction of the behaviour can be achieved by using numerical simulations.

**Master's Thesis goals:**

1. Review of automobile axles and possible situations that lead to their impact damage.
2. Assembly of the computational models of the welded rear axle and at least three obstacles.
3. Stress–strain analyses of impacts with various models of material.
4. Recommendations for safe vehicle operation based on the results obtained for various impact configurations.

**Recommended bibliography:**

DOWLING, N. E.; KAMPE, S. L. and KRAL, M. V. Mechanical Behavior of Materials: Engineering Methods for Deformation, Fracture, and Fatigue. 5th Ed. Harlow: Pearson Education Limited,2020. ISBN 978-1-292-27935-0.

JAZAR, R. N. Vehicle Dynamics: Theory and Application. 3rd Ed. Cham: Springer International Publishing AG, 2017. ISBN 978-3-319-53440-4.

LEE, D. and YANG, Ch. An analytical approach for design and performance evaluation of torsion beam rear suspension. Finite Elements in Analysis and Design. 2013, Vol. 63, pp. 98-106.

WU, S. R. and GU, L. Introduction to the explicit finite element method for nonlinear transient dynamics. Bohoken: John Wiley & Sons, 2012. ISBN 978-0-470-57237-5.

Deadline for submission Master's Thesis is given by the Schedule of the Academic year 2025/26

In Brno,

L. S.

| | |
|---|---|
| prof. Ing. Jindřich Petruška, CSc.<br>Director of the Institute | doc. Ing. Jiří Hlinka, Ph.D.<br>FME dean |

# ABSTRACT

This master's thesis deals with stress–strain analysis of a rear torsion axle colliding with foreign road obstacles. Following, the research about commonly used suspension systems including possible damage mechanisms and corresponding situations leading to structural failures, the theoretical fundamentals, covering the explicit formulation of the finite element method and material models of plasticity and ductile fracture, were presented. To simulate the impact, a comprehensive computational model was developed to cover a wide range of possible impact scenarios, varying in initial velocity magnitude, geometry of the obstacle, and position of the impact including a calibration of Johnson–Cook models of plasticity and ductile fracture. Subsequently, the comparison between all simulated scenarios was carried out, determining the impact on the possible fracture initiation. A material comparative study was presented comparing the calibrated Johnson–Cook model against a similar model found in the literature. Lastly, the accuracy of the computational model was validated using a controlled experiment utilizing a custom-built frame and a hydraulically-driven impactor.



# ABSTRAKT

Táto diplomová práca sa zaoberá napäťovo–deformačnou analýzou zadnej torznej nápravy automobilu pri náraze do cudzích cestných prekážok. Po uvedení bežne používaných systémov zavesenia kolies, vrátane možných mechanizmov poškodenia a príslušných situácií vedúcich k poruchám konštrukcie, boli predstavené teoretické základy, ktoré zahŕňali explicitné formulovanie metódy konečných prvkov a materiálové modely plasticity a tvárneho lomu. Pre simuláciu nárazu bol vyvinutý komplexný výpočtový model pokrývajúci širokú škálu možných scenárov nárazu, líšiacich sa veľkosťou počiatočnej rýchlosti, geometriou prekážky a polohou nárazu, vrátene kalibrácie modelov Johnson–Cook plasticity a tvárneho lomu. Následne boli výsledky porovnané s cieľom určiť vplyv na možnú iniciáciu trhliny. Neskôr bolo prezentované porovnanie nakalibrovaného Johnson–Cook modelu s podobným modelom získaným z dostupnej literatúry. Nakoniec bola kvalita výpočtového modelu validovaná pomocou riadeného experimentu využívajúceho na mieru vyrobený rám a hydraulicky poháňanú prekážku.



# KEYWORDS

torsion beam, explicit formulation of finite element method, crashworthiness, impact simulation, Johnson–Cook model, ductile fracture

# KĽÚČOVÉ SLOVÁ

torzná náprava, explicitná formulácia metódy konečných prvkov, odolnosť pri náraze, simulácia nárazu, Johnsonov–Cookov model, tvárny lom

# ROZŠÍŘENÝ ABSTRAKT

Táto diplomová práca sa zaoberá napäťovo–deformačnou analýzou zadnej torznej nápravy automobilu pri náraze do rôznych cestných prekážok. Vysokorýchlostný náraz je simulovaný pomocou explicitnej formulácie metódy konečných prvkov v softvéri LS-DYNA.

V prvej kapitole je predstavená problémová situácia, na ktorú nadväzuje samotná formulácia problému. Kapitola taktiež obsahuje definované hlavné ciele práce.

Druhá kapitola obsahuje prehľad najpoužívanejších systémov zavesenia kolies v súčasných automobiloch. Po vysvetlení základného princípu a hlavných častí zavesenia sú sformulované základné funkcie, ktoré musí zavesenie vykonávať. Následne sú predstavené jednotlivé typy zavesenia kolies. Podľa stupňa závislosti oboch kolies jednej nápravy sa zavesenia rozdeľujú do troch hlavných skupín: závislé, čiastočne závislé a nezávislé. V závere kapitoly sú predstavené a porovnané nápravy typu pevná náprava, torzná priečka s vlečnými ramenami, dvojité lichobežníkové zavesenie, zavesenie typu MacPherson a viacprvkové zavesenie. Kapitola taktiež obsahuje opis torznej nápravy z hľadiska najčastejších mechanizmov porúch spôsobujúcich trvalé poškodenie, spolu so scenármi vedúcimi k takýmto stavom. Ako je v práci diskutované, náraz do cudzej prekážky je jedným z najčastejších faktorov ohrozujúcich celkovú integritu torznej nápravy.

Tretia kapitola je venovaná teoretickým základom explicitnej formulácie metódy konečných prvkov a materiálovým modelom predikujúcim odozvu materiálu na aplikované zaťaženie. V prvej časti je predstavený základný princíp explicitnej metódy spolu s definíciou časového kroku, ktorým sa výpočet riadi. Taktiež je opísaný problém „hourglassingu“, na ktorom je vysvetlená nevyhnutnosť tlmenia tohto javu. Následne sú predstavené rozdiely medzi explicitnou a implicitnou metódou, ich vzájomné výhody, nevýhody a oblasti aplikácie, pre ktoré sú určené. Druhá časť kapitoly sa zameriava na materiálové modely plasticity a tvárneho lomu. Okrem multilineárneho modelu plasticity a modelu konštantného lomového pretvorenia, ktoré sa radia medzi jednoduchšie prístupy, je pozornosť venovaná najmä Johnson–Cook modelu. Hlavnou výhodou tohto modelu je, že do výpočtu plasticity a tvárneho lomu zahŕňa vplyv rýchlosti deformácie, triaxiality napätia a teploty.

Štvrtá kapitola obsahuje detailný postup tvorby výpočtového modelu, pomocou ktorého bol simulovaný vysokorýchlostný náraz. Keďže neexistuje veľa štúdií zaoberajúcich sa podobnou tematikou, zámerom tejto práce bolo vytvoriť spoľahlivý základ, ktorý by dostatočne zodpovedal reálnej situácii. Geometria torznej nápravy, prevzatá od priemyselného partnera, bola transformovaná na škrupinový model. Následne boli definované tri rôzne geometrie prekážok s využitím jednoduchých, ľahko definovateľných geometrických tvarov: prekážka v tvare trojuholníka s ostrým hrotom, plochá prekážka v tvare hranola a prekážka v tvare sféry. Pre zachytenie čo najširšieho spektra možných situácií bol náraz simulovaný v dvoch rôznych výškových polohách. Pre vernú simuláciu reálneho zavesenia bolo nevyhnutné korektne definovať nelineárne charakteristiky pružín a tlmičov.

Keďže pre simuláciu bola k dispozícii len samotná geometria nápravy, bolo nutné zahrnúť zotrvačné vlastnosti celého vozidla. To sa dosiahlo rozdelením hmotnosti na odpruženú a neodpruženú časť. Odpružená časť predstavuje hmotnosť automobilu pripadajúcu na nápravu. S cieľom zachytiť najnepriaznivejší scenár bola simulovaná hmotnosť plne

naloženého vozidla, implementovaná úpravou hustoty pomocných telies na hornej strane tlmičov a pružín. Neodpružená hmotnosť (hmotnosť kolies a brzdového systému) bola zahrnutá pomocou funkcie "mass point".

Následne boli definované jednotlivé stupne voľnosti a okrajové podmienky v miestach kontaktu nápravy s rámom karosérie. Pomocným telesám na hornej časti pružín a tlmičov bol umožnený len posuv v smere pohybu nápravy, pričom vertikálny pohyb samotného rámu vozidla bol zanedbaný. V miestach puzdier ložísk v prednej časti nápravy bola okrem posuvu umožnená aj rotácia. Prekážka bola modelovaná ako nepohyblivé tuhé teleso. V rámci simulácií sa porovnávali tri rôzne počiatočné rýchlosti: 20 km/h, 50 km/h a 90 km/h.

Kapitola taktiež obsahuje detailnú kalibráciu materiálových modelov Johnson–Cook na základe údajov z ťahových skúšok. Vzhľadom na použitie relatívne veľkých elementov bolo rozhodnuté, že na opis plasticity sa použije multilineárny model, keďže aproximácia mocninnou funkciou vykazovala zreteľné odchylky. Vplyv rýchlosti deformácie a triaxiality napätia bol však zahrnutý do modelu tvárneho lomu, využívajúc dáta z ťahových skúšok pri zvýšených rýchlostiach a skúšok vzoriek s vrubom.

Posledná kapitola obsahuje porovnanie výsledkov spolu s validáciou výpočtového modelu prostredníctvom uskutočneného experimentu. Najskôr bol analyzovaný vplyv rýchlosti nárazu, geometrie prekážky a vertikálnej polohy miesta nárazu. Z porovnania vyplynulo, že trojuholníková prekážka predstavuje najkritickejší stav, keďže minimálna styková plocha takmer okamžite iniciuje vznik trhliny. Naopak, prekážka v tvare sféry sa vďaka hladkému povrchu a kontinuálne sa zväčšujúcej kontaktnej ploche ukázala ako najbezpečnejšia, keďže ani pri najvyššej počiatočnej rýchlosti nebolo dosiahnuté lomové plastické pretvorenie. Pri posúdení vplyvu počiatočnej rýchlosti sa preukázalo, že s narastajúcou rýchlosťou vozidla sa zmenšuje plastická zóna v okolí miesta nárazu. Ďalej bol posúdený vplyv vertikálnej polohy miesta nárazu. Z výsledkov vyplýva, že nižšia pozícia znížila kontaktnú silu pri náraze v priemere o približne 38 %, čo priamo ovplyvňuje množstvo disipovanej kinetickej energie do štruktúry nápravy. Ukázalo sa, že výraznejší vplyv na možnú iniciáciu trhliny než samotná rýchlosť automobilu má miesto nárazu a geometria prekážky. Toto tvrdenie potvrdzuje fakt, že trojuholníková prekážka spôsobila trhlinu vo všetkých simulovaných prípadoch, zatiaľ čo pri sférickej prekážke sa trhlina neobjavila ani pri najkritickejšom nastavení. Kapitola taktiež obsahuje porovnanie kalibrovaného materiálového modelu s podobným modelom prevzatým z dostupnej literatúry. Porovnanie preukázalo len minimálne rozdiely v rozložení plastických pretvorení, hoci boli materiálové modely kalibrované na rôzne aplikácie s použitím odlišnej siete konečných prvkov. Diplomová práca je zakončená validáciou vytvoreného modelu pomocou riadeného experimentu, simulujúceho náraz hydraulicky poháňaným impaktorom. Do výpočtového modelu boli implementované nevyhnutné úpravy na dosiahnutie cieľovej rýchlosti a maximálnej kontaktnej sily. Následne bol deformovaný tvar porovnaný s naskenovanou geometriou. Aj napriek použitiu idealizovaných okrajových podmienok, ktoré nezohľadňovali tlmenie a flexibilitu experimentálneho rámu, boli rozdiely v deformácii minimálne, v rozsahu približne 1–2 mm.

## CITATION

BODO, Ondrej. *Stress-strain analysis of the impact of the automobile rear axle on the road obstacle*. Brno, 2026. Available also at: https://www.vut.cz/en/students/final-thesis/detail/166250. Master's Thesis. Brno University of Technology, Faculty of Mechanical Engineering, Institute of solid mechanics, mechatronics and biomechanics. Supervised by doc. Ing. František Šebek, Ph.D.

## AUTHOR'S DECLARATION

I hereby declare that I have written this master's thesis on my own, under the supervision of doc. Ing. František Šebek, Ph.D., using the literature included in the list of references.

In Brno on 22. 5. 2026 .....

Bc. Ondrej Bodo

## USE OF ARTIFICIAL INTELLIGENCE

Generative AI tools (Google Gemini, Anthropic Claude, DeepL Translate) were used during the preparation of this thesis in a limited scope for the following purposes: correction of the English text (grammar, punctuation, and word order) and assistance in developing the computational model in LS-DYNA (specifically, identifying correct commands and keywords).

AI was not used to generate expert conclusions or replace work with primary sources. All outputs were critically reviewed and verified by the author, who bears full responsibility for the content of this thesis.

## ACKNOWLEDGEMENT

I would like to express my sincere gratitude to my supervisor, doc. Ing. František Šebek, Ph.D., for his valuable comments and professional expertise, which were essential to the successful completion of this thesis.

# CONTENTS

**1 INTRODUCTION** **19**
1.1 Motivation . . . 19
1.2 Formulation of the problem situation . . . 20
1.3 Problem formulation and solution . . . 20
1.4 Goals of the thesis . . . 21

**2 OVERVIEW OF VEHICLE SUSPENSION SYSTEMS** **23**
2.1 Suspension systems . . . 23
2.2 Functions of suspension systems . . . 24
2.3 Types of suspension systems . . . 24
2.3.1 Solid axle . . . 25
2.3.2 Torsion beam . . . 25
2.3.3 Double wishbone . . . 25
2.3.4 MacPherson strut . . . 25
2.3.5 Multi-link . . . 26
2.4 Damage mechanisms of torsion beam suspension . . . 27
2.4.1 Possible failure mechanisms of torsion beam suspension and contributing situations . . . 27

**3 FUNDAMENTALS OF THE EXPLICIT FINITE ELEMENT METHOD AND MATERIAL MODELS** **29**
3.1 Explicit formulation of finite element method . . . 29
3.1.1 Basic principles . . . 29
3.1.2 Critical time step value . . . 30
3.1.3 Hourglassing . . . 30
3.1.4 Difference between explicit and implicit approach . . . 31
3.2 Models of plasticity and ductile fracture . . . 31
3.2.1 Multilinear plastic hardening model . . . 32
3.2.2 Model of constant fracture strain . . . 32
3.2.3 Johnson–Cook strength and failure model . . . 32

**4 CREATION OF THE COMPUTATIONAL MODEL** **35**
4.1 Geometry and selection of obstacles used . . . 35
4.2 Simulation settings . . . 39
4.2.1 Finite element mesh . . . 39
4.2.2 Connections . . . 40
4.2.3 Inertial properties and mass distribution . . . 42
4.2.4 Kinematic constrains and initial conditions . . . 43
4.3 Calibration of material models . . . 46
4.3.1 Derivation of the stress–strain curve . . . 46
4.3.2 Calibration of the plastic hardening model . . . 49
4.3.3 Calibration of the failure model . . . 51

**5 RESULTS AND DISCUSSION** **59**
5.1 Analysis of impact scenarios . . . . . 59
5.1.1 Influence of obstacle geometry . . . . . 59
5.1.2 Influence of impact velocity . . . . . 62
5.1.3 Influence of vertical position . . . . . 64
5.1.4 Comparative summary of simulated impact scenarios . . . . . 66
5.2 Material model comparative study . . . . . 67
5.3 Validation with impact experiment . . . . . 70

**6 CONCLUSION WITH SUGGESTIONS FOR FUTURE STUDIES** **75**

**BIBLIOGRAPHY** **80**

**LIST OF FIGURES** **82**

**LIST OF TABLES** **83**

**A APPENDIX** **85**

# 1 INTRODUCTION

## 1.1 Motivation

The suspension system is a key part of the whole vehicle structure that connects a car's chassis to its rotating wheels and therefore directly influences the ride comfort for all passengers inside the vehicle. The whole system should represent a harmony between various components, such as spring stiffness, damping capacity of the shock absorber, and the geometry of the suspension mechanism itself. Thereby, providing a right balance between ride comfort, road handling, and load-carrying capacity. As a result, different types of vehicles require different suspension settings to prioritize the primary function for which the vehicle is designed.

However, in addition to functional requirements, the suspension design process must also take into account development constraints such as manufacturing costs, design complexity, and development time. Although automotive engineers always strive to ensure the highest possible levels of safety and driving performance, these goals must be balanced against economic considerations, as an increased number of design iterations and prototype tests directly leads to higher costs and longer development times. From this perspective, suspension design concepts that combine sufficient functional performance with structural simplicity are highly desirable. A typical example of such a solution is the rear torsion bar suspension, which represents a favorable compromise between cost, robustness, and driving performance. By effectively utilizing the material and mechanical properties of the torsion bar, this design arrangement maintains partial independence of rear-wheel movement while providing sufficient vehicle handling and acceptable ride comfort for mass-produced vehicles.

Throughout its life, the torsion beam suspension undergoes various stress states and operating conditions that could cause a potential problem in overall integrity of the suspension body resulting in cracks initiations or other problems potentially weakening suspension's functionality. Stated problems can be caused by vibrations from driving over road irregularities, fatigue damage from constantly fluctuating torsional stress, or direct impact of the axle to various road obstacles.

With a combination of controlled experimental testing and computational modeling using numerical simulations, one can predict the behavior of such system under various conditions and determine whether its functionality is impaired.

## 1.2 Formulation of the problem situation

The structural integrity of the torsion rear axle plays a significant role in vehicle safety and long-term reliability. Throughout its service life, the torsion beam is frequently subjected to various high-velocity loading impacts, particularly on unpaved or poorly maintained roads causing the vehicle to strike stones, debris, or other obstacles. Considering the rear axle is often the first structural part of the vehicle to sustain a direct impact, a better understanding of its structural response is essential for defining safe operational limits and improving overall crashworthiness of a vehicle.

Sufficiently predicting the material degradation or immediate ductile fracture requires a high-fidelity approach utilizing dynamic computational modeling, as these situations are often accompanied by steep plastic strain and stress gradients occurring at high strain rates.

## 1.3 Problem formulation and solution

Initially, in Chapter 2, research is conducted on commonly used suspension systems, covering their related advantages and disadvantages, along with brief insights into possible damage mechanisms of a rear torsion beam suspension and the situations that could lead to such failures.

Chapter 3 provides the fundamental theoretical knowledge of the explicit formulation of the finite element method, including material models of plasticity and ductile fracture, which are subsequently applied in the computational simulations.

Chapter 4 describes the development of the computational model of the rear torsion beam suspension, featuring impact scenarios that vary in initial velocity magnitude, obstacle geometry, and different vertical placements of an obstacle. Additionally, Chapter 4 includes the practical calibration of the required material models based on provided experimental uniaxial tests.

Finally, Chapter 5 provides a comprehensive assessment of the structural response across the simulated impact configurations by validating the influence of each input variable on the possibility of fracture initiation. The chapter concludes with a material sensitivity study comparing the calibrated Johnson–Cook material model against a similar model found in existing scientific literature, followed by a validation of the obtained results from numerical simulations against a controlled physical experiment.

## 1.4 Goals of the thesis

1. Review of automobile axles and possible situations that lead to their impact damage.

2. Assembly of the computational models of the welded rear axle and at least three obstacles.

3. Stress–strain analyses of impacts with various models of materials.

4. Recommendations for safe vehicle operation based on the results obtained from various impact configurations.

# 2 OVERVIEW OF VEHICLE SUSPENSION SYSTEMS

The purpose of this chapter is to cover basic and essential aspects of suspension systems by describing their functions, desired features, and different types used in today's vehicles. More detailed information about this topic can be found in the literature included in the bibliography.

## 2.1 Suspension systems

Both the front and rear suspensions are fundamental parts of the overall vehicle structure, as they connect the rotating wheels to the car's chassis, allowing relative motion between them to ensure comfort while keeping the wheels in contact with the ground.

As shown in Figure 2.1, a vehicle suspension consists of four main components, such as *mechanism*, *shock absorber (dumper)*, *spring*, and *bushing*.

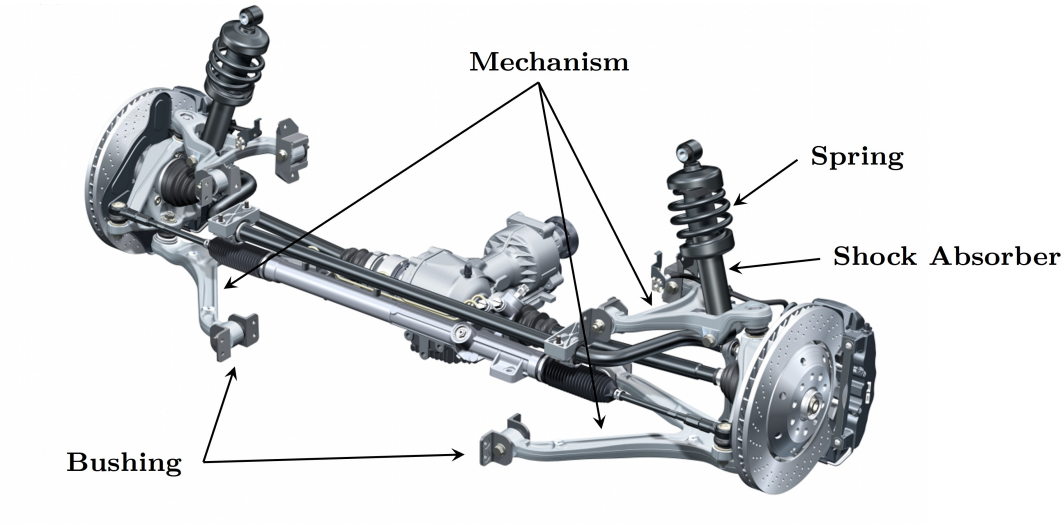



Figure 2.1: The main components of a suspension system [4]

The primary role of the suspension mechanism is to transfer all forces and moments between the vehicle body and the ground through one or several control arms. It determines a relative motion between them and defines the suspension geometry. The shock absorber is used to dissipate the kinetic energy generated by the wheel travel, thereby damping the suspension oscillations. However, an overly effective damper can compromise the vehicle's ride quality as well as handling. The spring (a winding wire or a number of metal strips) supports the vehicle's weight and its stiffness can very effectively influence the ride comfort for passengers. Using stiffer springs improves the vehicle's handling but negatively impacts the ride comfort, and vice versa. The bushing is placed in between two metal objects to prevent direct contact in order to minimize vibrations and unwanted noise [12].

## 2.2 Functions of suspension systems

The suspension must satisfy a number of requirements which are partially in conflict, therefore the suspension settings directly influence the vehicle's overall dynamic behavior on the road. These three key principles have a significant impact on the vehicle's behavior.

- **Ride Comfort**
  Defined by the suspension system's ability isolate the cabin of a moving vehicle from road-induced disturbances. It can be qualified by the level of vibration transmitted into the passenger cabin.
- **Road Holding**
  The ability of the suspension system to withstand both lateral and longitudinal forces generated by driving, thereby maintaining consistent contact between tires and the ground to allow for optimal cornering, traction, and braking performance.
- **Handling**
  Ensuring vehicle stability during maneuvering by predictably, proportionally, and smoothly following the acceleration, breaking, and steering inputs [18].

## 2.3 Types of suspension systems

The selection of a suspension system can significantly influence the vehicle's dynamic behavior by balancing load capacity, driving performance, and manufacturing cost. Based on the degree of dependability of each wheels on the same axle, suspension systems can be categorized into *dependent* (e.g., solid axle), *semi-independent* (e.g., torsion beam), and *independent* (e.g., MacPherson strut, double wishbone, multi-link). This section presents the most used configurations in the automotive industry, ranging from simple but robust solid axle to high-performance multi-link suspension.

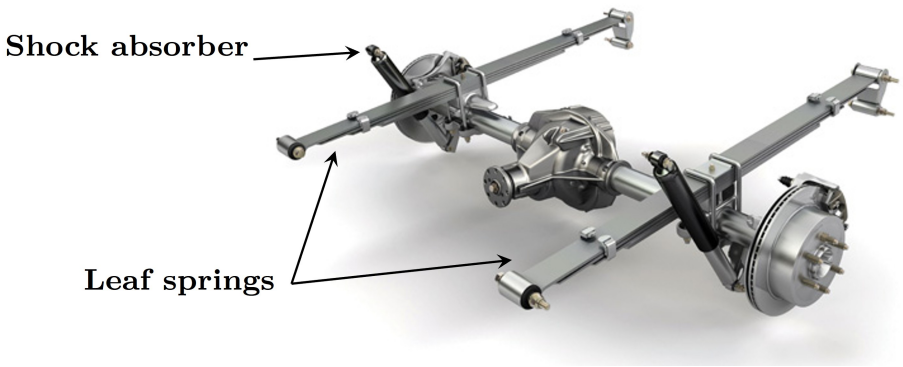



Figure 2.2: The solid axle suspension with leaf springs [9]

### 2.3.1 Solid axle

The solid axle suspension uses a rigid beam with wheels mounted on both sides and can be paired with either coil or leaf springs (see Figure 2.2). This system is mostly used in trucks or vans due to its high load-carrying capacity and durability. However, because both wheels are connected to a single rigid bar, any movement of one wheel is directly transmitted to the other, which compromises ride comfort and handling [12].

### 2.3.2 Torsion beam

The torsion beam (as shown in Figure 2.3) is the most popular rear suspension for modern compact, front–wheel–drive cars due to its simplicity, efficiency, and low weight. It consists of two trailing arms connected by a flexible torsion bar, which absorbs all forces and moments while also replacing an anti-roll bar. As a semi-independent system, it offers less flexibility compared to fully independent and more expensive systems. However, it remains sufficient for most lightweight vehicles, offering an excellent price-performance ratio [11].

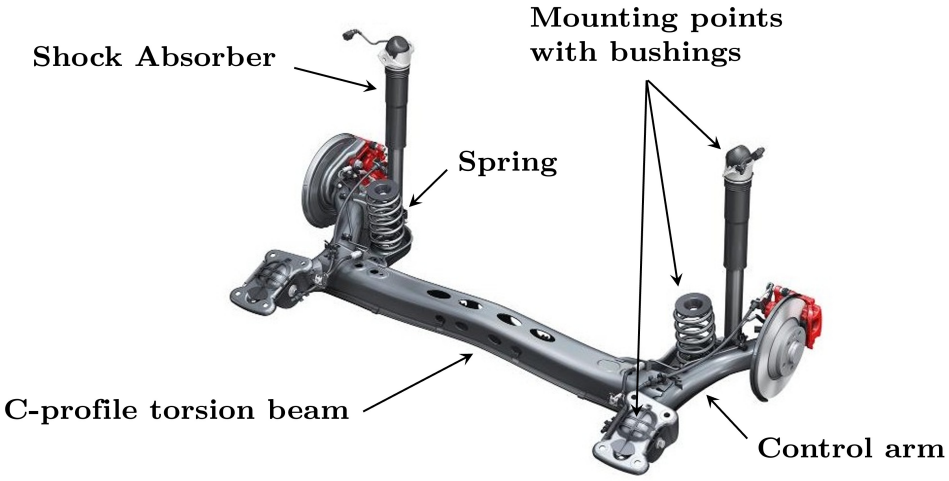



Figure 2.3: The torsion beam suspension with highlighted parts [6]

### 2.3.3 Double wishbone

The double wishbone suspension utilizes two A-shaped arms on the upper and lower side of the wheel hub to maintain optimal wheel orientation throughout the suspension travel (see Figure 2.4). This feature improves handling and road holding. Therefore, it is a preferred solution for both high-performance and luxury vehicles [6].

### 2.3.4 MacPherson strut

The MacPherson strut is one of the most popular front suspension systems in modern cars, as it combines both a shock absorber and a coil spring into a single telescopic strut. This unit is rigidly connected to the wheel hub to absorb vertical forces from the road, while the lower control arm bears the lateral and longitudinal forces. This type of independent suspension is cheaper and lighter than the double wishbone configuration [6].

Comparison between the MacPherson strut (on the left side) and the double wishbone suspensions is shown in Figure 2.4.

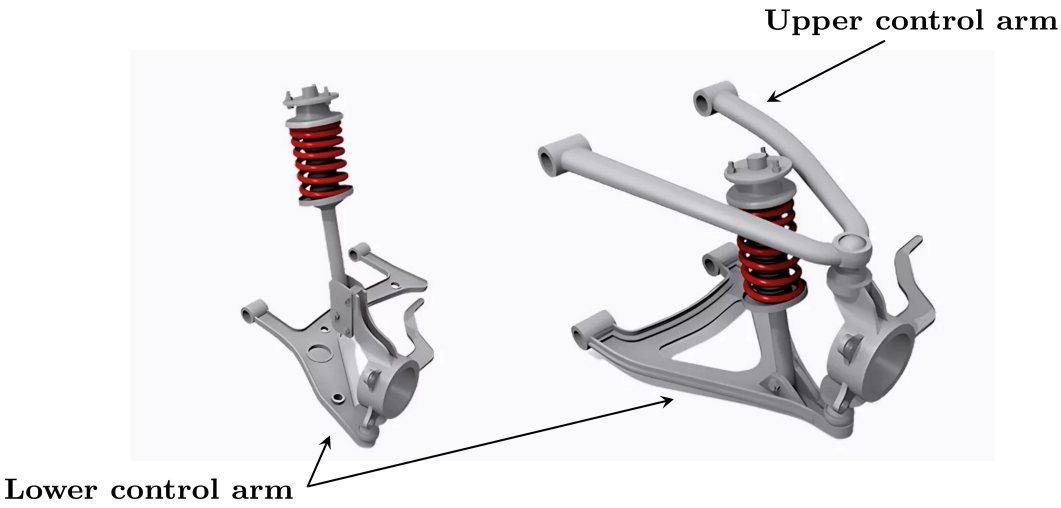



Figure 2.4: Comparison between the MacPherson strut and the double wishbone suspension [20]

### 2.3.5 Multi-link

The multi-link system (shown in Figure 2.5) utilizes several control arms to connect the wheel hub to the vehicle's chassis, offering unparalleled flexibility in tuning the suspension. Having full control over the wheel's movement allows for a superior driving experience and therefore this suspension is primarily used in high-performance or track-focused cars [6].

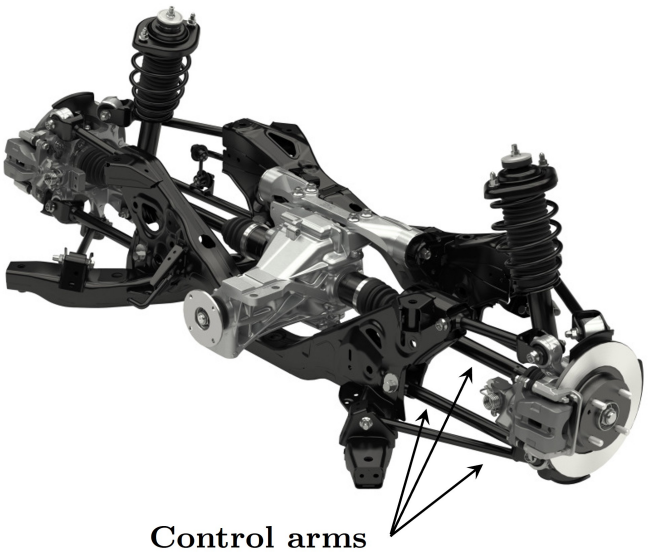



Figure 2.5: Multilink suspension with highlighted control arms [6]

## 2.4 Damage mechanisms of torsion beam suspension

In order to fully understand the structural behavior of a torsion beam rear suspension under various loading conditions, it is necessary to analyze the system's principal strengths and weaknesses. Meaning reviewing possible damage mechanisms with corresponding real-world scenarios that may lead to such structural failure.

### 2.4.1 Possible failure mechanisms of torsion beam suspension and contributing situations

As described in Section 2.3, the torsion beam suspension consists of two trailing arms connected by a flexible beam, which should be able to withstand large torsional displacement without failure to allow each wheel to move independently over road bumps, while also providing enough stiffness to support lateral forces of moving vehicle during cornering. Therefore, the torsion beam is most damage-sensitive component of such system, and its stiffness has a significant influence on the overall handling and durability of the vehicle.

Another factor contributing to the sensitivity of the torsion beam suspension is its placement within the overall vehicle structure, which increases the risk of direct contact with unknown object that could potentially damage the torsion beam itself.

The most common reason a torsion beam suspension is damaged or its functionality is compromised are road bumps and other road obstacles that could collide with the moving car. Another reason is when a suspension is exposed to alternating loads from cornering, as well as accelerating or braking. This can lead to fatigue damage over time in regions of stress concentrations. With an increase of load cycles, initial microcracks can gradually propagate, creating a fracture that could compromise the reliability of the entire suspension system.

Yuzhuo et al. [16] studied mechanisms of crack initiation of rear axle during accelerated life testing by comparing cars with and without replaced new rear axle. They compared both vehicles on different road surfaces and also simulated road vibrations by electromagnetic exciters to establish the correlation between the vibration frequency of rear axles and vibrations caused by road irregularities to determine fatigue life for both rear axles.

This thesis is focused on situations when the axle is damaged by a direct impact by a road obstacle or when the axle is in direct contact with a foreign object. The most common objects that could potentially weaken the axle's structure are stones or other debris typically found on unpaved roads. Furthermore, driving over uneven terrain or hitting deep potholes can significantly reduce the ground clearance, causing the lowest point of the suspension to come to the direct contact with the road surface.

# 3 FUNDAMENTALS OF THE EXPLICIT FINITE ELEMENT METHOD AND MATERIAL MODELS

This chapter is dedicated to the fundamental theoretical knowledge that will later be implemented in computational simulations. The chapter is primarily focused on describing explicit formulation of the finite element method (FEM) and also material models of plasticity and ductile fracture, which can predict the behavior of material under applied load exceeding its yield strength.

## 3.1 Explicit formulation of finite element method

The explicit formulation of FEM is ideal for certain types of engineering problems for its specific properties. It is a powerful tool for simulating highly nonlinear or dynamic situations such as explosions or crash tests.

The first use of explicit simulations dates back to 1960s and 1970s. However, with advancements of computational capabilities over the years, the complexity of problems that can be solved using explicit simulations have expanded dramatically. Today, explicit solvers are implemented in all widely used software, including ABAQUS (Abaqus/Explicit) or ANSYS (LS-DYNA).

### 3.1.1 Basic principles

The principle of the explicit method is based on the second Newton's law transcribed to its matrix form and defined at a specific time $t$:

$$\ddot{\mathbf{U}}_t = \mathbf{M}^{-1}\left(\mathbf{F}_t^{ext} - \mathbf{F}_t^{int}\right) \tag{3.1}$$

where $\ddot{\mathbf{U}}_t$ is the vector of nodal acceleration at a time $t$, $\mathbf{M}$ is the global weight matrix, $\mathbf{F}_t^{ext}$ is the vector of external forces and $\mathbf{F}_t^{int}$ is the vector of internal forces.

A nodal displacement matrix $\mathbf{U}_{t+\Delta t}$ given at time $t + \Delta t$ (where $\Delta t$ is the size of one time step) is then calculated by the central difference method from known values of nodal acceleration as follows:

$$\dot{\mathbf{U}}_{t+\frac{\Delta t}{2}} = \dot{\mathbf{U}}_{t-\frac{\Delta t}{2}} + \ddot{\mathbf{U}}_t \frac{\Delta t_t + \Delta t_{t+\Delta t}}{2} \tag{3.2}$$

$$\mathbf{U}_{t+\Delta t} = \mathbf{U}_t + \dot{\mathbf{U}}_{t+\frac{\Delta t}{2}} \Delta t_{t+\Delta t} \tag{3.3}$$

where $\dot{\mathbf{U}}_{t+\frac{\Delta t}{2}}$ is a matrix of nodal velocity given at time $t + \frac{\Delta t}{2}$, $\dot{\mathbf{U}}_{t-\frac{\Delta t}{2}}$ is a matrix of nodal velocity given at time $t - \frac{\Delta t}{2}$ and $\mathbf{U}_t$ is a matrix of nodal displacement given at time $t$.

Afterwards, the new geometrical configuration is calculated by adding the nodal displacement to an existing initial configuration at each time step. Stress and strain values of

each element are then computed from known values of nodal displacement, velocity, and acceleration and constitutive equations. The whole process is repeated until the total simulation time is reached.

A full detailed explanation and derivation of the explicit finite element method is available in [19] and [7].

### 3.1.2 Critical time step value

The main disadvantage of an explicit algorithm over an implicit one is the fact that the explicit algorithm is stable on one condition. In order to ensure the calculation stability, the time step must not exceed its critical value ($\Delta t^{crit}$), which is calculated as follows:

$$\Delta t \leq \Delta t^{crit} = \frac{l}{c} \tag{3.4}$$

where $l$ is a characteristic dimension of an element and $c$ is a longitudinal wave velocity, which is given as:

$$c = \sqrt{\frac{E}{\rho}} \tag{3.5}$$

where $E$ is Young's modulus and $\rho$ is a material density.

The critical time step value is defined as time that is required for the stress wave to pass through the smallest element and is automatically set by the solver before starting the calculation. Therefore, it is highly desirable and important to have a homogeneous mesh throughout the model, as one significantly smaller element can substantially increase the solution time [7].

### 3.1.3 Hourglassing

Hourglassing is a numerical phenomenon which typically occurs in under-integrated[1] hexahedral or quadrilateral elements in dynamic finite element simulations. It is zero-energy deformation mode with zero stiffness, that creates "zig–zag" distortions in the mesh resembling an hourglass as it is depicted in Figure 3.1. The effect should always be minimized, because it can potentially destroy the result's validity by dominating the global deformation.

[1] Elements utilizing only one Gaussian integration point. The use of such elements can decrease the computational time, but allows for creation of hourglass modes, requiring artificial stabilization. Detailed explanation of the issue can be found in [5].

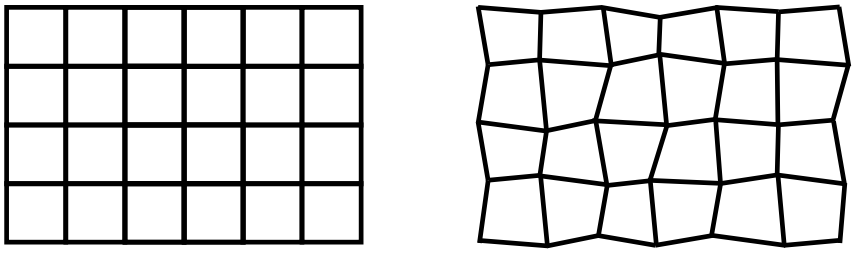


Figure 3.1: Deformed geometry with a pronounced hourglass effect

To ensure numerical stability, the hourglass energy must be monitored and it should not exceed a threshold of 5 % of the model's total internal energy, which is a standard industry practice. This phenomenon can be controlled by distributing the external loads across multiple nodes, refining the finite element mesh (can increase the computational time), or using fully integrated element formulation. While the use of fully integrated elements naturally eliminates the effect, it also comes with a risk of over-stiffening the model and potentially leading to shear or volumetric locking. Other methods, which are commonly used in finite element sofware to control the hourglass effect, are adding artificial viscous damping or artificial stiffness to the model [21].

### 3.1.4 Difference between explicit and implicit approach

The most significant difference between both approaches, as stated before, is the fact that the explicit formulation is conditionally stable, whereas the implicit one is stable regardless of the time step length.

On the other hand, an explicit algorithm has a significant advantage in its ability to express the global weight matrix as a diagonal matrix, making the resulting system of equations mutually independent. Another advantage of explicit algorithm is that the time requirement rises linearly with the increase in the number of mesh nodes used, unlike the implicit algorithm, where it rises quadratically.

## 3.2 Models of plasticity and ductile fracture

To achieve a high-fidelity numerical simulation, the material model must accurately represent the mechanical response of the material from initial elastic behavior through to possible structural failure. This section provides a brief comparative overview of simplified models of plastic hardening (*multilinear plastic hardening model*) and ductile fracture (*linear damage accumulation model*) with more comprehensive *Johnson–Cook strength and failure model*. The Johnson–Cook was specifically selected for its ability to incorporate the influence of stress triaxiality, strain rate, and temperature on material behavior and it is widely used across the automotive industry.

### 3.2.1 Multilinear plastic hardening model

The multilinear plastic hardening model represents the stress–strain response as a series of piecewise linear intervals. This is the main difference from the simple bilinear model, which accounts only for a constant tangent modulus after the yield point. The multilinear model is able to capture more gradual and detailed plastic hardening of a given material by dividing the curve into multiple segments.

To capture the material response after the yield stress, the model utilizes a dependency of the equivalent stress $\sigma_{eq}$ on the equivalent plastic strain $\overline{\varepsilon}_p$.

### 3.2.2 Model of constant fracture strain

It is the simplest form of failure observation. The fracture occurs when the equivalent plastic strain $\overline{\varepsilon}_p$ reaches its preset critical value $\varepsilon^f$. The damage parameter $D$ is then expressed as follows:

$$D = \frac{\overline{\varepsilon}_p}{\varepsilon^f} \tag{3.6}$$

Even though later studies have shown that the damage is not linear with respect to the equivalent plastic strain, this criterion is still widely used in commercial finite element software for its simplicity and understandability.

### 3.2.3 Johnson–Cook strength and failure model

The plasticity model, which was published in 1983 by Johnson and Cook [13], has became popular for solving problems involving high velocity or large displacement. The model was first formulated to determine the effect of strain rate, temperature and pressure on the strain to fracture.

The plasticity model is expressed as a function of the equivalent plastic strain, the temperature $T$ and the plastic strain rate $\dot{\varepsilon}_p$ and it is defines as follows:

$$\sigma_{eq} = [A + B(\overline{\varepsilon}_p)^n] \left[1 + C\ln\left(\frac{\dot{\varepsilon}_p}{\dot{\varepsilon}_0}\right)\right] \left[1 - \left(\frac{T - T_0}{T_{melt} - T_0}\right)^m\right] \tag{3.7}$$

where $\sigma_{eq}$ is the equivalent stress, $\dot{\varepsilon}_0$ is the reference plastic strain rate, $T_0$ is the room temperature, $T_{melt}$ is the material melting temperature and $A$, $B$, $C$, $n$ and $m$ are material constants. The first bracket on the right side of the equation (3.7) describes quasi-static stress–strain relation at temperature $T_0$, the second bracket accounts for strain rate hardening and the last one captures the temperature dependence.

After the plasticity model, they continued their research in 1985 by defining the failure function, which determine the fracture strain [14].

The fracture model is defined as a fracture strain $\varepsilon^f$, which is expressed as function of the stress triaxiality $\eta$, the plastic strain rate and the temperature:

$$\varepsilon^f = [D_1 + D_2\exp(D_3\eta)] \left[1 + D_4\ln\frac{\dot{\varepsilon}_p}{\dot{\varepsilon}_0}\right] \left[1 + D_5\frac{T - T_0}{T_{melt} - T_0}\right] \tag{3.8}$$

where $D_1$, $D_2$, $D_3$, $D_4$ and $D_5$ are material constants. The stress triaxiality is a dimensionless pressure dependence parameter and it is defined as:

$$\eta = \frac{\sigma_m}{\overline{\sigma}} \tag{3.9}$$

where $\sigma_m$ is the mean (hydrostatic) stress, which is defined as an average of all principal stresses and $\overline{\sigma}$ is the von Mises equivalent stress.

The failure occurs when the damage parameter $D$ (see equation (3.6)) equals $D = 1$.

# 4 CREATION OF THE COMPUTATIONAL MODEL

This chapter presents the development and configuration of the computational model required for a comprehensive behavior analysis of the rear torsion beam axle under an impact with a road obstacle. The accuracy of the simulation is directly tied to the model's geometric representation, component properties, and boundary conditions. The objective is to create a computationally robust and efficient model reflecting a physical system, while incorporating necessary simplifying assumptions to make the numerical simulations reproducible.

## 4.1 Geometry and selection of obstacles used

This thesis was conducted in cooperation with an industry partner, which provided the geometry of the analyzed rear torsion beam axle, as well as details regarding its spatial orientation to simulate the realistic behavior of a fully loaded moving vehicle. Figure 4.1 depicts the geometry of the rear axle with basic dimensions.

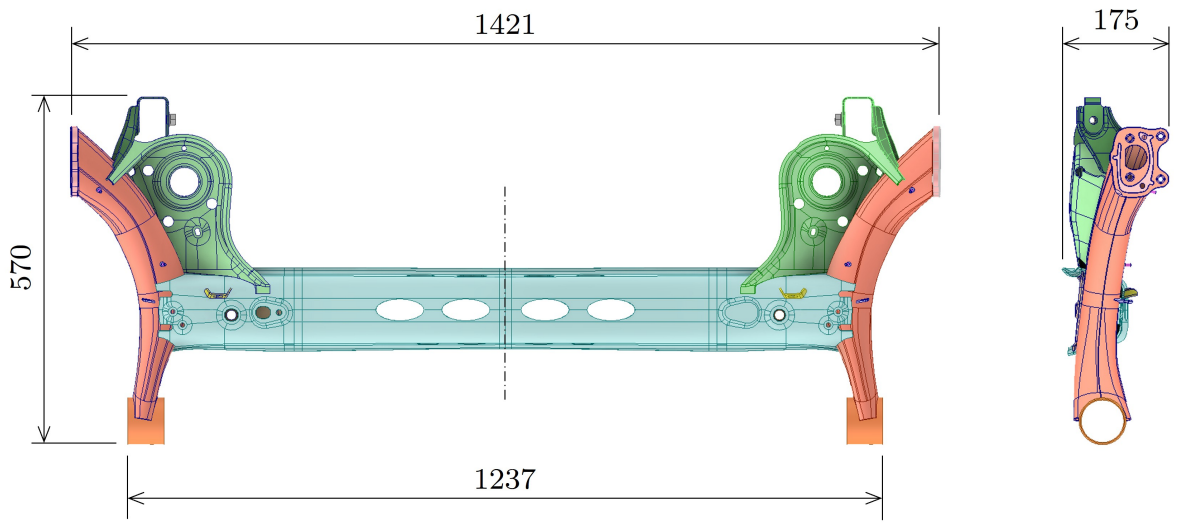



Figure 4.1: Geometry of analyzed rear torsion beam axle with dimensions in mm

To reduce computational time and simplify the simulation, and since the axle is an assembly of welded sheet-metal parts with different but constant thickness, the solid geometry was transformed into a surface model with defined thicknesses. The original solid geometry was also stripped of unnecessary parts such as mounts for electrical cables and hydraulic hoses or other accessories. Figure 4.2 shows a detailed view of the axle geometry after its transformation into a surface model.

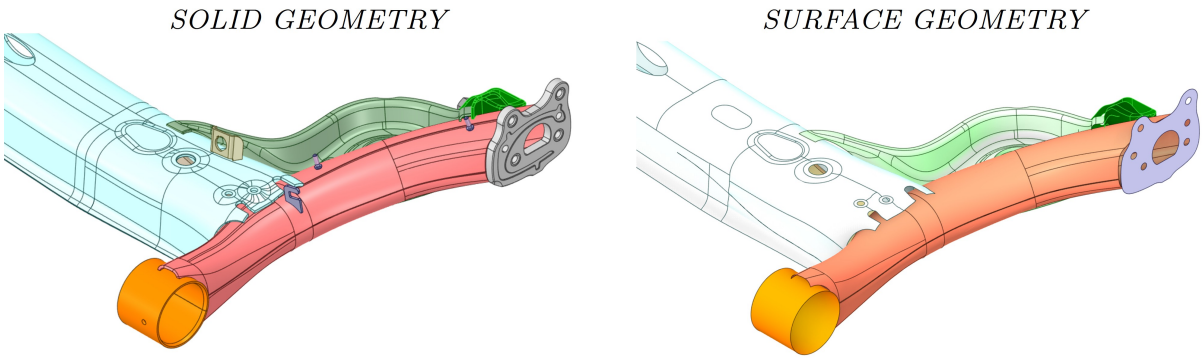



Figure 4.2: Comparison between the original solid geometry and the resulting surface geometry of the rear torsion beam axle

In real-life road conditions, obstacles that could potentially collide with a moving vehicle are nearly impossible to define due to notable differences in shape, size, orientation, and material properties. For this reason, the intention was to select standardized and simple shapes rather than highly specific or complex geometries to make the simulations representative. To replicate a wide range of different types of obstacles that could directly impact a car's rear axle, three representatives were chosen (shown in Figure 4.3). The main reason for this selection was the difference in contact areas at the initial stage of impact. The assumption was that the sharp triangular obstacle (shown in Figure 4.3, middle) would represent the most critical scenario, in contrast to the spherical obstacle (shown in Figure 4.3, right). The rectangular shape, which can represent a brick or a piece of timber on the road, was added to compare possible differences and to obtain more information about the torsion beam's behavior under impact.

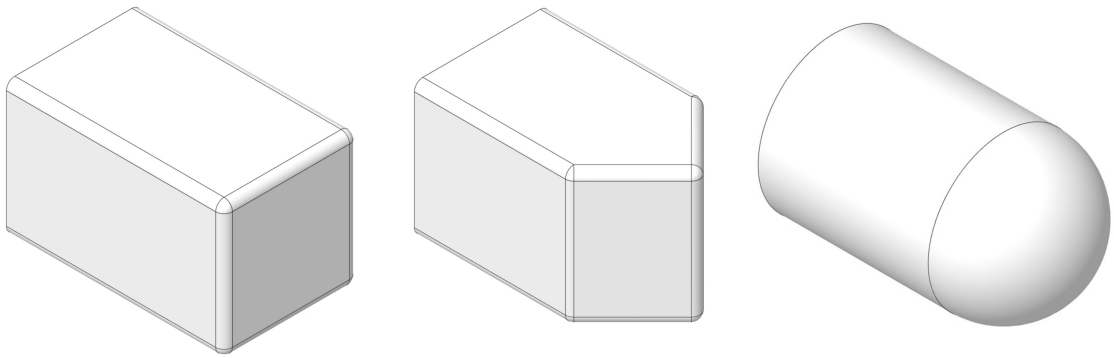


Figure 4.3: Models of all used obstacles

To prevent possible problems with the penetration of the obstacle to the torsion beam under impact and to keep the geometry of the obstacles representative without sharp edges, a radius of 5 mm was added to all edges possibly colliding with the axle as it is depicted in Figure 4.3. Figure 4.4 shows the detailed geometry of the chosen obstacles.

The intention was to keep the overall dimensions the same to ensure the results are comparable.

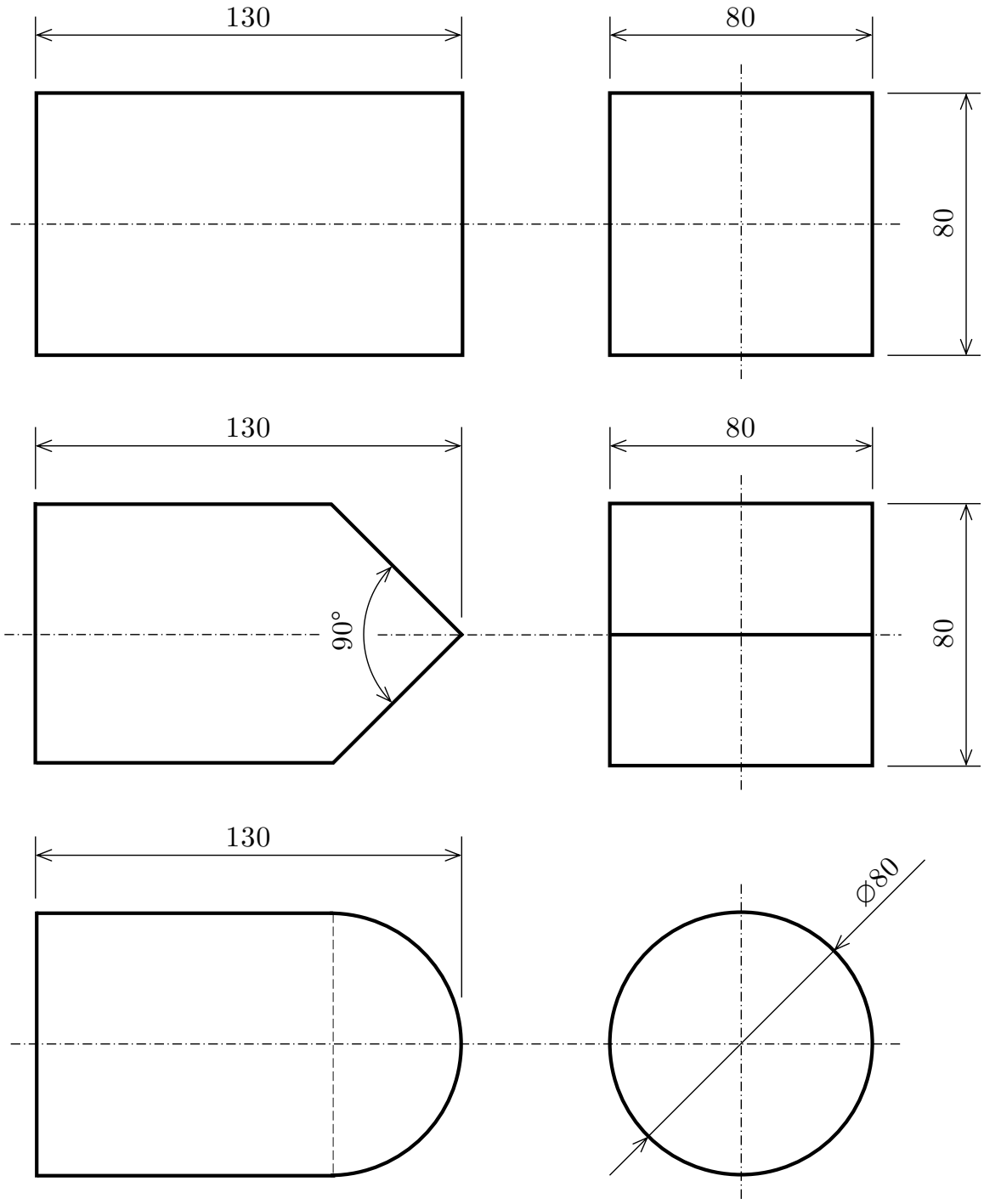



Figure 4.4: Geometry of all used obstacles

The obstacle should come into direct impact with the axle in the location that would most likely initiate the crack. The exact location was determined based on previous tests done by the industrial partner. Figure 4.5 shows a top view of the obstacle positioning.

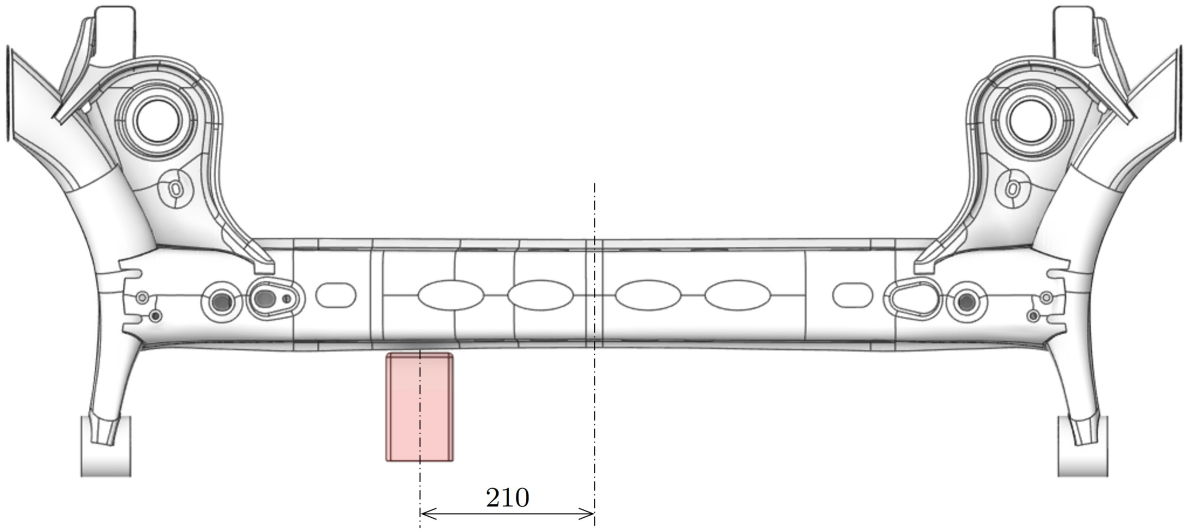



Figure 4.5: Placement of the obstacle from the top view

To simulate a wider range of potential impact scenarios and gain a broader understanding of the structural response of the axle, the vertical placement of the obstacle was set at two different heights with a difference of 25 mm, as it is depicted in Figure 4.6.

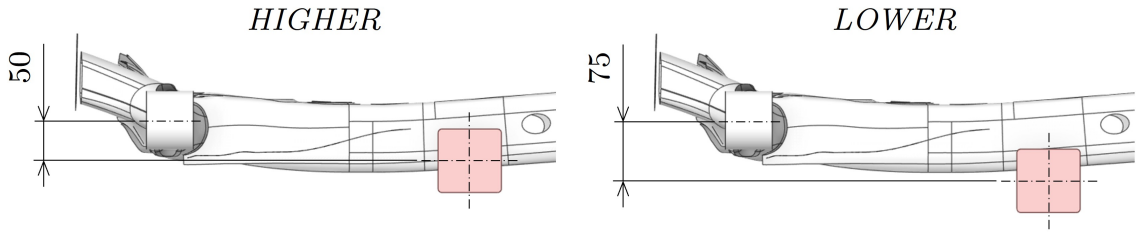



Figure 4.6: Comparison between two vertical placements of the obstacle

## 4.2 Simulation settings

All simulations were performed using the LS-RUN 2025 R1 software running the LS--DYNA solver. The initial simulation preparation was done in LS-DYNA module in the ANSYS Workbench 2025 R1 software to facilitate the geometry import and the implementation of fundamental boundary conditions. Subsequently, the simulation input KEY file was generated for import into the dedicated LS-DYNA software (LS-Prepost 4.12), which offers more extensive configuration options for explicit LS-DYNA project.

### 4.2.1 Finite element mesh

As stated in Section 4.1, the assembly of the torsion beam axle was transformed from solid to surface geometry. The model was discretized using linear shell elements with a global size of 4 mm. To accurately capture the stress and strain gradients around the contact zone, local mesh refinement was applied to achieve a 1 mm element size, as it is depicted in Figure 4.7.

To avoid the hourglassing phenomenon described in Subsection 3.1.3, an hourglass control formulation was implemented. For the shell elements, the control type 4 (Flanagan–Belytschko stiffness form) within the `*HOURGLASS` keyword was selected.

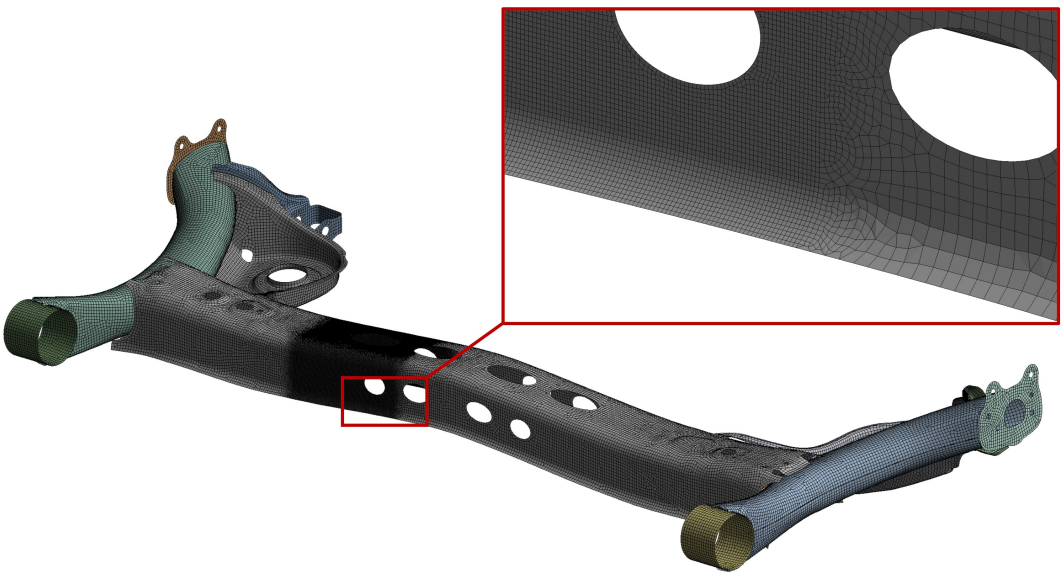


Figure 4.7: Finite element mesh of used torsion beam axle

The shell thickness of each component of the axle was set according to the obtained solid geometry. For example, the shell thickness of the main C-profile torsion beam was 3.2 mm. To capture realistic behavior of sheet metals by shell elements, the number of through-thickness shell integration points was set to three to obtain the stress–strain characteristics of both sides as well as the midsurface of any given part.

Figure 4.8 shows the finite element mesh of all used obstacles with visibly softened sharp outer edges as it was discussed above. Similar to the axle, the size of the elements was set to 4 mm.

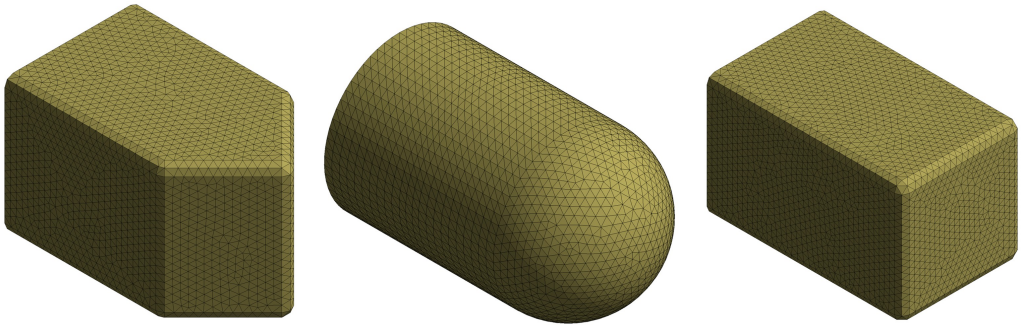


Figure 4.8: Finite element mesh of all selected obstacles

### 4.2.2 Connections

#### Contacts

Since the rear torsion beam axle is an assembly of welded sheet metal parts, bonded contacts were used to replicate the joints. Specifically, the contact keyword `*CONTACT_TIED_NODES_TO_SURFACE_OFFSET` was selected. As the name of the keyword suggests, each welded joint was realized by the nodes of an outside edge to its adjacent surface.

Additionally, the contact type `*CONTACT_AUTOMATIC_SURFACE_TO_SURFACE` was used between the torsion beam and the road obstacle to model the actual impact. This contact type can automatically detect the interaction between two predefined surfaces. Coefficients of static (`FS`) and dynamic friction (`FD`) were assigned values of 0.3 and 0.2, respectively, in accordance with common practice for representing the steel-on-concrete contact.

#### Spring and shock absorber

Accurate definition of spring and shock absorber characteristics is essential for capturing the axle's dynamic behavior. Without taking both components into consideration, the simulation would not faithfully represent real-life scenarios.

As shown in Figure 4.9, both components were placed between auxiliary bodies and remote points. The use of remote points was chosen to represent the mounting system of the spring and the shock absorber on the rear axle body. The keyword `*CONSTRAINED_NODAL_RIGID_BODY` was used in both situations, which connects a selected set of nodes into a single rigid entity with one master node by which the other boundary conditions can be applied. In both cases, the node sets were selected according to where the spring or the shock absorber is in contact with the obtained axle geometry.

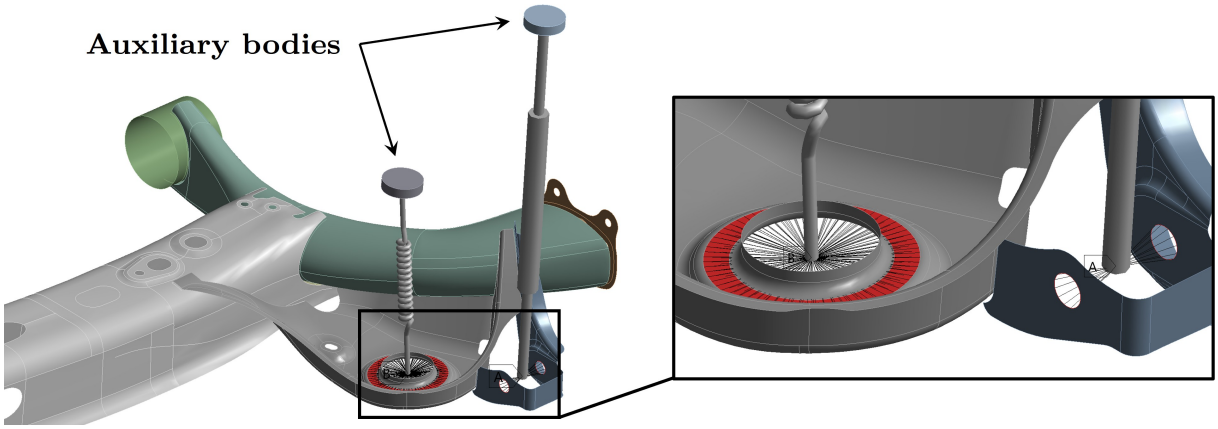



Figure 4.9: Placement of the spring and the shock absorber

Placement of the auxiliary bodies corresponds to the exact mounting locations of the spring and the shock absorber on the vehicle's chassis. The simulation captures the orientation of the axle, the spring pretension and the placement of the mounting points of the spring and the damper under the vehicle's fully loaded condition, as specified by the industrial partner. This setup reflects the worst-case scenario in terms of the distance between the axle and the road surface, as well as the reduced suspension travel.

Both components were modeled using the `*SECTION_DISCRETE` and the `*ELEMENT_DISCRETE` keywords defining the section and the element type, respectively. As shown in Figure 4.10 on the left side, the linear spring was modeled so that only compression is enabled. The reason for this change was to keep the minimum distance between the axle and an imaginary road surface that was predefined by the initial placement of the axle. Consequently, the spring material was defined as nonlinear constraining the positive displacement of the spring (elongation) using the `*MAT_SPRING_NONLINEAR_ELASTIC (*MAT S04)`. Additionally, the value of the spring's pretension was taken into account by shifting the linear response of the spring. The magnitude of the pretension was calculated as the length difference between the free length of the spring and the actual operating length multiplied by the spring's stiffness coefficient. The values of both the free length of the spring and its stiffness coefficient were obtained from the industrial partner. The shock absorber was also modeled as nonlinear according to the provided information. Therefore, the `*MAT_DAMPER_NONLINEAR_VISCOUS (*MAT S05)` keyword was used for material modeling with a defined force versus displacement-rate relationship depicted on the right side in Figure 4.10.

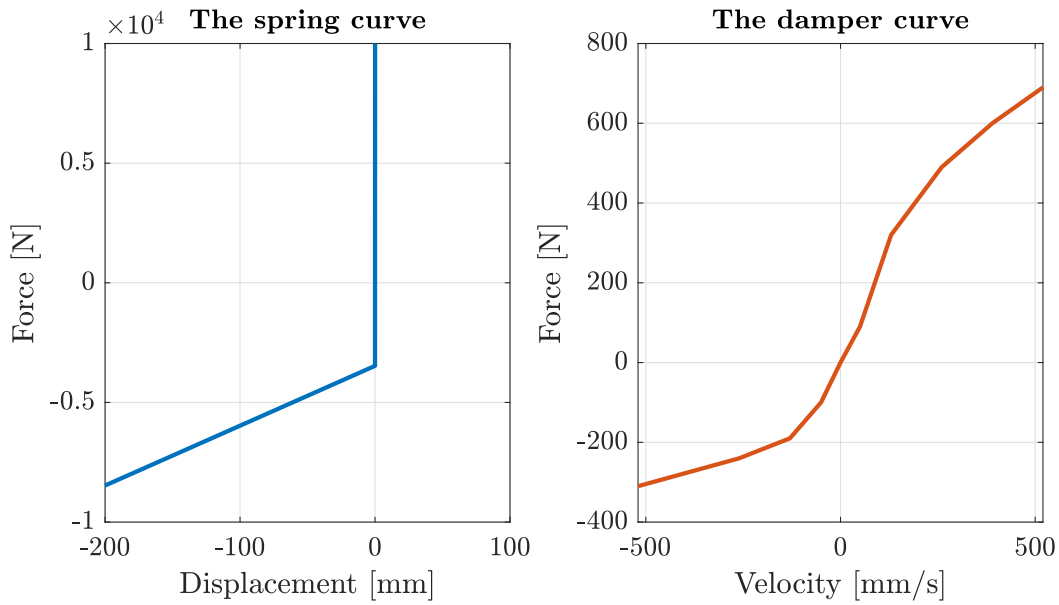



Figure 4.10: Defined nonlinear curves for the spring and the damper

### 4.2.3 Inertial properties and mass distribution

To ensure the simulation correctly represents a dynamic impact with a road obstacle, it is necessary to account for vehicle mass and its distribution to achieve accurate inertial properties and values of kinetic energy.

For the purposes of this simulation, two types of mass were added to adequately replace the behavior of the entire moving car. First was the sprung mass, which is the part of the vehicle's total mass that is supported by the suspension. According to the information received from the industrial partner and considering the fact that the simulation reflected the worst-case scenario in terms of maximum allowable load, the mass of 1680 kg was equally distributed, as the mass of the entire car, to all four rigid auxiliary bodies (shown in Figure 4.9) by adjusting their mass density. This addition accounts only for correct inertial properties. The second type was the unsprung mass, which includes the weight of all components attached to the suspension such as brakes and the entire wheel mounting system including the wheel itself. As it is depicted in Figure 4.11, similar to the spring attachment, the mass point was added as a rigid entity connecting four wheel mounting holes using the `*CONSTRAINED_NODAL_RIGID_BODY` keyword. A mass of 30 kg, representing the estimated weight of a single wheel assembly including the braking system, was assigned to a newly defined node on each side of the axle using the `*ELEMENT_INERTIA` keyword.

Additionally, the `*LOAD_BODY_Z` keyword was used to enable the gravity effect, which utilizes a defined acceleration constant to apply a uniform gravitational force by multiplying the model's total mass.

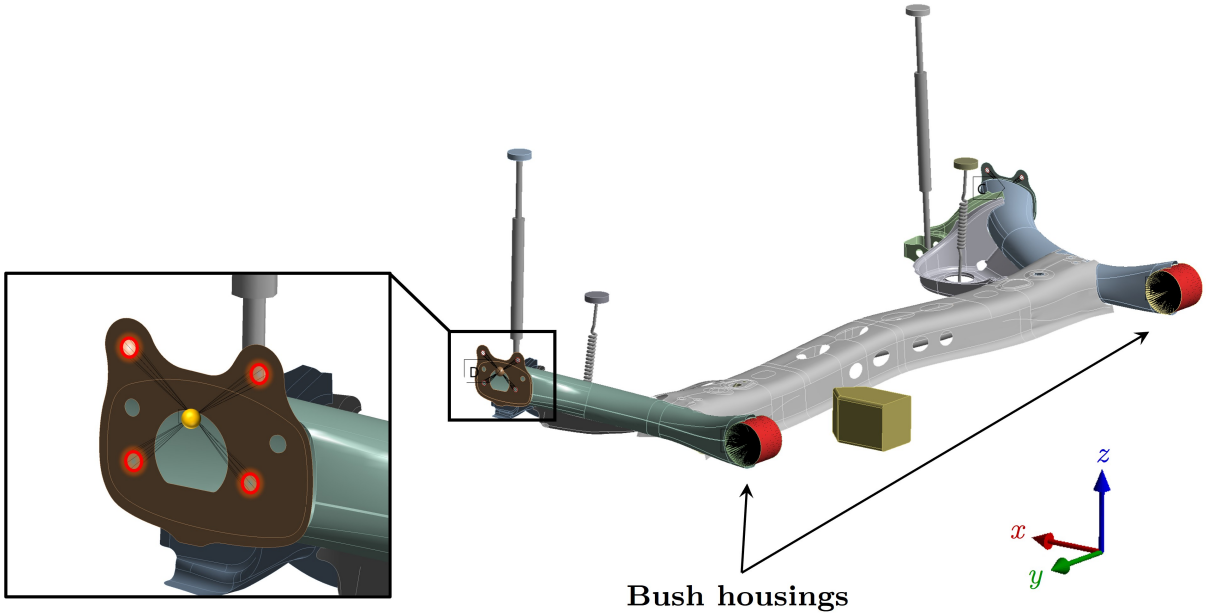



Figure 4.11: Model of used torsion beam suspension with detailed view of the wheel mount

### 4.2.4 Kinematic constrains and initial conditions

Kinematic boundary conditions were constructed to correspond as closely to the real behavior of the rear torsion beam axle as possible. All used boundary conditions were selected to accurately represent the relative motion between the axle, the road surface and the vehicle chassis. This study presumes the chassis to be a perfect rigid body throughout the simulation maintaining constant distances between each mounting point.

Both front bush housings, the only points at which the axle directly contacts the vehicle's chassis (shown in Figure 4.11), were modeled as rigid bodies using `*MAT_RIGID (*MAT 020)` keyword. This reflects the fact that any potential deformation of the housing around the bearing and bushing would be minimal and was therefore disregarded for the purposes of this study. Defining the material as `*MAT_RIGID (*MAT 020)` enabled for setting the kinematic boundary conditions inside of the material keyword itself by using newly defined node in the centre of the rigid body inertia. By setting the `CON1` parameter to 5, the translational degrees of freedom (DOFs) in the $y$ and the $z$ axes were set to zero due to the previously described presumption, that the vehicle's chassis stays rigid and maintains its vertical stability during the modeled simulation. The longitudinal translational DOF (in the direction of the axle movement) parallel to the $x$ axis was left unrestricted. As for rotational DOFs, setting the next parameter `CON2` to 6 left only the rotation around the $y$ axis unconstrained allowing for a natural behavior of the bearing.

Other locations where the suspension interacts with the vehicle's chassis are the mounting points of the spring and the shock absorber on each side. The auxiliary bodies (shown in Figure 4.9) served as the interface through which all boundary conditions were established. All DOFs on the auxiliary bodies were controlled by the `*BOUNDARY_PRESCRIBED_MOTION_RIGID` keyword, due to the fact that each body was set to be rigid using the `*MAT_RIGID`

(*MAT 020) material model. Therefore, the boundary conditions could be applied to the one predefined node same as the spring and the shock absorber were connected to. To comply with the assumption of a rigid and stable[1] chassis, only the translational DOFs in the direction of the $x$ axis (the direction of the axle movement) was set as free, constraining all other translational as well as all rotational DOFs.

Subsequently, the displacement in the longitudinal direction of all points of contact between the suspension and the car's chassis (the front bush housing and the auxiliary bodies used as the mounting points of the spring and the shock absorber) on both sides was coupled. This was achieved using the *CONSTRAINED_JOINT_REVOLUTE keyword, which constrains the relative motion of two rigid bodies to rotations about a defined axis. First, two auxiliary bodies on one side were combined into one rigid entity using the *CONSTRAINED_RIGID_BODIES, which can then be constrained using the revolute joint. Next, two sets of coincident nodes were created at both sides of each bush housing to define the centerline axis about which the revolute joint allows the rotation. One node from each coincident pair was assigned to the rigid bush housing, while the second node was attached to the newly defined rigid entity consisting of both auxiliary bodies. This configuration ensured a constant distance between the two rigid bodies throughout the simulation time.

Finally, the obstacle was set as a rigid immovable object by applying the boundary condition restricting all translational DOFs to all its nodes using the *BOUNDARY_SPC_SET keyword. This setup allowed for detailed study of the worst-case scenario since the obstacle was not able to deform or absorb kinetic energy, providing the most conservative approach to test the torsion axle's crashworthiness.

To provide a better understanding of all boundary conditions used, Figure 4.12 shows all specific locations where the constraints were implemented by highlighting the unconstrained DOFs ($UX$ stands for displacement in the $x$ axis and $ROTY$ stands for rotation about the $y$ axis) including the direction of the initial velocity ($VX$). Furthermore, the black lines connect the chassis mounting points with linked $UX$ responses.

As for the predefined initial conditions, the same non-zero initial velocity in the negative $x$ axis direction was prescribed to all moving parts, including the axle assembly itself with all four auxiliary bodies defining the mounting places of the spring and the damper. This thesis studied three initial velocity magnitudes **20 km/h**, **50 km/h**, and **90 km/h** to cover a wider range of the axle's operative conditions and to obtain a better understanding of the axle's response and behavior. For this purpose, the *INITIAL_VELOCITY_GENERATION and *INITIAL_VELOCITY_RIGID_BODY keywords were used.

[1] Negligible displacement in the direction of the $z$ (vertical) axis.

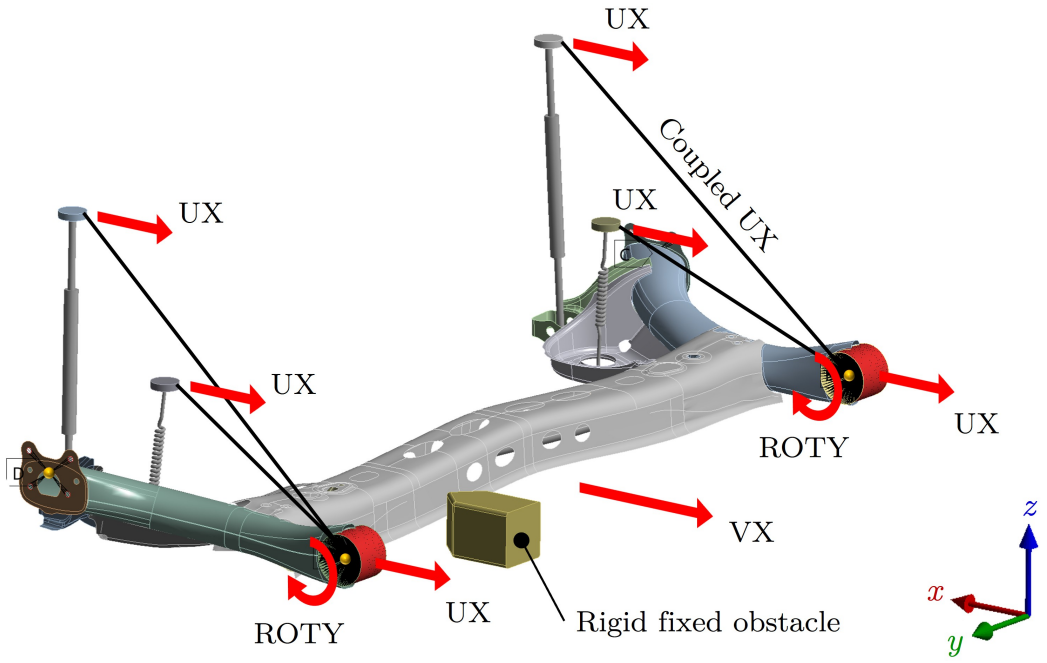



Figure 4.12: Model of boundary conditions with highlighted directions of unconstrained degrees of freedom at specific locations

To reduce computational time, the termination times were adjusted based on the magnitudes of the initial velocity using the `*CONTROL_TERMINATION` keyword. The termination times were calculated to ensure the axle had sufficient time to fully pass through the fixed obstacle. The specific termination time values for each initial velocity are listed in the Table 4.1.

Table 4.1: Defined termination times for varying initial velocity magnitudes

| **Velocity magnitude** [km/h] | 20 | 50 | 90 |
|---|---|---|---|
| **Termination time** [s] | 0.070 | 0.030 | 0.015 |

A comprehensive description along with a detailed explanation of the input parameters for the keywords used in this thesis can be found in **LS-DYNA Keyword User's Manual, Volume I** [3].

## 4.3 Calibration of material models

This section provides a detailed description of the calibration of the material models for the torsion beam of the suspension assembly, based on results from performed dynamic and quasi-static tensile tests. The section consists of theoretical framework and the practical realization of obtaining the stress–strain curve. Subsequently, the calibrations of the plastic hardening model and the failure model are presented.

### 4.3.1 Derivation of the stress–strain curve

Obtaining the accurate stress–strain curve is a critical step in calibrating the material models required for subsequent simulations. This process requires considerable attention to ensure the calibrated models represent physical reality as reliably as possible.

#### Theoretical background

The initial step is to recalculate stresses and strains retrieved from experimental tensile tests, which are in engineering form, to true stresses and true strains. To verify the accuracy of the calibrated curve, numerical simulations are conducted to validate the results against experimental data.

Strain is the basic deformation quantity, and its engineering form is defined according to

$$e = \frac{L - L_0}{L_0} = \frac{\Delta L}{L_0} \tag{4.1}$$

where $L$ represents the length of the deformed specimen and $L_0$ is the initial undeformed length. This is a unitless quantity and sometimes can be expressed as a percentage, in which case the value is multiplied by 100.

Engineering stress is defined as a force $F$ applied on an initial undeformed cross-sectional area $S_0$, and it is expressed as

$$s = \frac{F}{S_0} \tag{4.2}$$

Both engineering expressions may be viable for brittle materials with negligible plasticity; however, they are not sufficient for large deformations in ductile materials. Therefore, it is necessary to formulate true expressions of stress and strain.

True (logarithmic) strain is defined using the length increment $\mathrm{d}L$ as

$$\mathrm{d}\varepsilon = \frac{\mathrm{d}L}{L} \tag{4.3}$$

After integration from the initial point $L_0$ to the endpoint $L$, the expression for the true strain stands as

$$\varepsilon = \ln\frac{L}{L_0} \tag{4.4}$$

True stress (see Equation 4.5) is defined as a force $F$ applied on the actual deformed area $S$. This approach is needed for the stress formulation of ductile materials where the cross-sectional area is shrinking due to large plastic deformation.

$$\sigma = \frac{F}{S} \tag{4.5}$$

Recalculations between engineering and true values (see Equation 4.6 and 4.7) are possible assuming the deformation is uniform. This presumption is correct up to the tensile (ultimate) strength of the material $R_m$, which is the maximum force load the material can withstand, after which the necking occurs [10].

$$\varepsilon = \ln(1 + e) \tag{4.6}$$

$$\sigma = s(1 + e) \tag{4.7}$$

To obtain the flow curve values[2] exceeding the tensile strength, several correction methods have been developed. These methods determine true stresses and strains beyond the necking, where the stress state deviates from uniaxial and uniform conditions. Among the various procedures proposed, the most widely used are the Bridgman correction, introduced by Bridgman in 1952 [8], or the MLR correction, developed by La Rosa in 2003 [15], which was enhanced by Mirone in 2004 [17].

### Practical realization

First step is to perform an experimental tensile test, which serves as a benchmark. After obtaining the dependence of the force reaction on the displacement of the specimen, the engineering quantities were calculated (see Equations 4.1 and 4.2). Consequently the true quantities can be evaluated using Equations 4.6 and 4.7 until the point of plastic stability ($R_m$). The following course and slope of the curve is estimated iteratively, when after every iteration the force–displacement dependence from the numerical simulation is compared to the experimental data. The flow curve is corrected until the deviation is minimized.

The tensile tests were performed on specimens created from the C-profiled torsion beam, since this part has the highest probability of colliding with foreign road obstacles. The following figure shows geometry for smooth specimen used in experimental tests.

[2]The flow curve is a name of the material input for numerical simulations utilizing a multilinear plastic hardening model (see Subsection 3.2.1). It defines the relationship between equivalent stress and equivalent plastic strain.

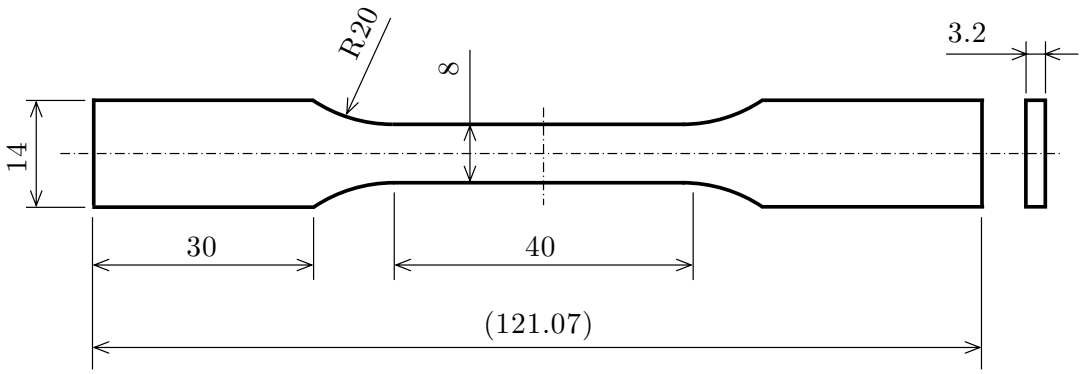



Figure 4.13: Geometry of the smooth specimen used for experimental tensile test

Subsequently, the numerical simulation was conducted using finite element mesh with global size of 1 mm to match the mesh on the global model of full rear suspension around the point of the contact. The choice of element size was a compromise between model's accuracy and computational time of full simulation. Figure 4.14 shows model used in numerical simulation along with boundary conditions. To shorten the computational time, symmetry was used along both axis. Similar to the global model, simulation was conducted in LS-PrePost software running the LS-DYNA explicit solver. Additionally, to maintain consistency with the global model, shell elements were used with a thickness of 3.2 mm, along with hourglass control formulation (`*HOURGLASS`, type 4) to ensure simulation stability. The simulation was performed under displacement control to match the failure displacement obtained from experiment. The length of 15 mm was set due to the fact that the initial length $L_0$ used in experimental test was 30 mm.

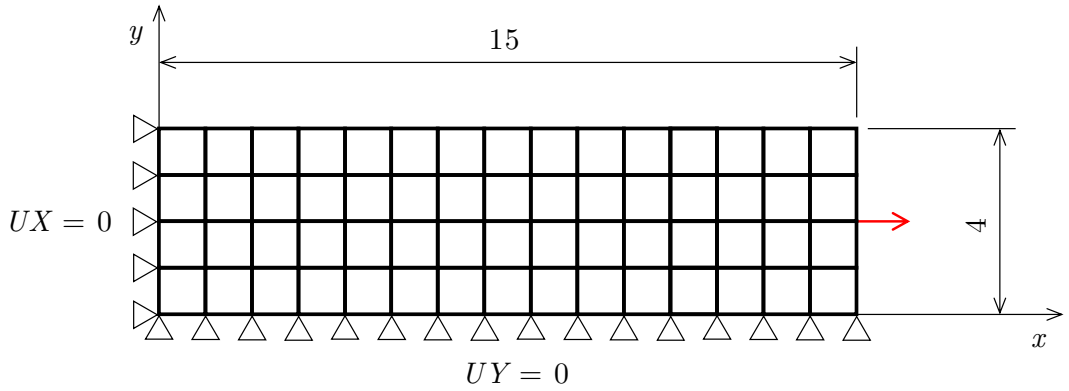



Figure 4.14: Finite element mesh and boundary conditions used in the tensile test simulation of the smooth specimen

The flow curve was calibrated manually using the trial and error method. Figure 4.15 shows how accurate the numerical simulation described real tensile test where the experimental curve was calculated as an average of two performed tensile tests. Visible deviation

appeared in the necking area where the relatively big element could not sufficiently mimic the changing geometry. The calibrated flow curve is shown in Figure 4.16 (the blue line).

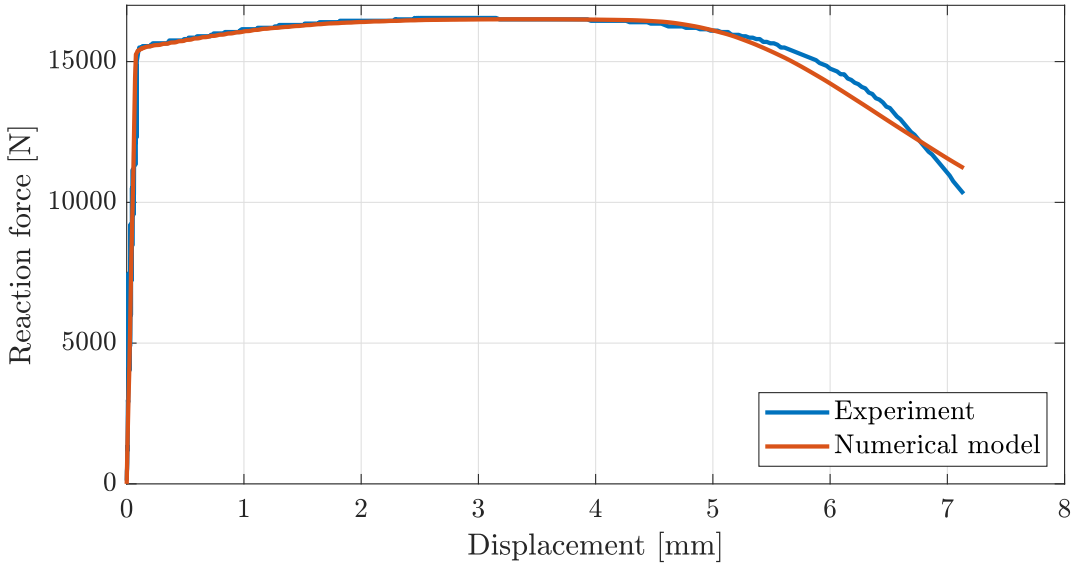



Figure 4.15: Comparison of force reaction–displacement dependencies for the smooth specimen

### 4.3.2 Calibration of the plastic hardening model

To determine the parameters of the Johnson–Cook plasticity model (see Equation 3.7), the calibrated flow curve displayed on Figure 4.16 must first be approximated by the function obtained from the first bracket of Equation 3.7, describing quasi-static stress–strain relation at room temperature. Through this process, the $A$, $B$ and $n$ material parameters, which are listed in Table 4.2, were derived by fitting the plasticity model to the numerical data using MATLAB's nonlinear least-squares regression.

Table 4.2: Calibrated material parameters for the Johnson–Cook plasticity model

| $\boldsymbol{A}$ [MPa] | $\boldsymbol{B}$ [MPa] | $\boldsymbol{n}$ [–] |
|---|---|---|
| 546.19 | 353.16 | 0.32 |

Due to the relatively large elements used, a significant error occurred in the model approximation (the red line in Figure 4.16). Because of this non-negligible deviation, it was decided to use a simpler multilinear plastic hardening model, which does not take the effects of strain rate and temperature into account. This decision was supported by the fact that, after obtaining experimental tensile tests at higher strain rates, the deviation in reaction force values was not substantial, therefore, a more accurate description

of plastic hardening is more important for this simulation than the strain rate effect. However, the strain rate effect was incorporated into the failure model calibrated in following subsection, due to a visible difference in the maximum displacement. Figure 4.17 illustrates the reaction force–displacement dependencies for two quasi-static tests with a strain rate of $\dot{\varepsilon}_{sta}(t) = 5.6 \cdot 10^{-4}$ s$^{-1}$ and two dynamic tests with a higher strain rate of $\dot{\varepsilon}_{dyn}(t) = 5.6 \cdot 10^{-1}$ s$^{-1}$.

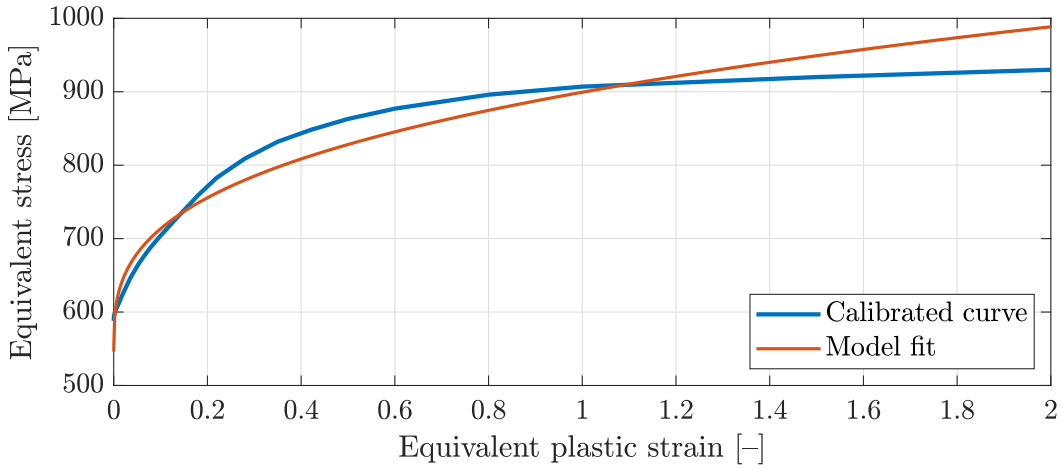



Figure 4.16: Multilinear equivalent stress–equivalent plastic strain curve approximated by Johnson–Cook power law function

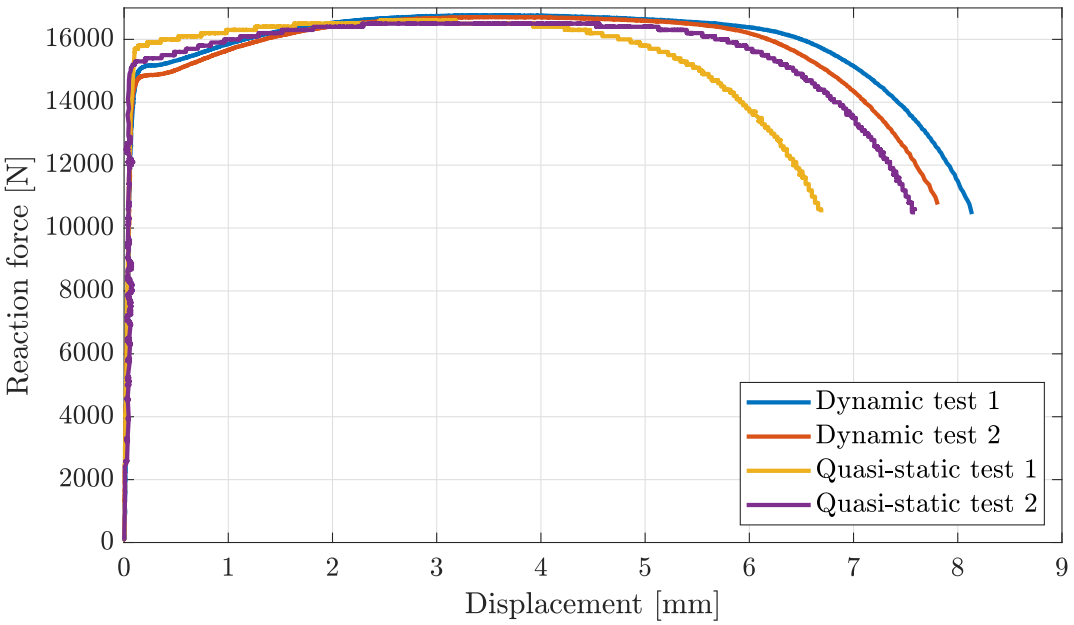



Figure 4.17: Comparison of reaction force–displacement dependencies of quasi-static and dynamic tests

### 4.3.3 Calibration of the failure model

Accurate calibration of the failure model is a key part of predicting the material behavior under simulated loads. For this study, the Johnson–Cook failure model was selected due to its more sophisticated approach than the basic model of constant fracture strain. Unlike the simple damage model, the Johnson–Cook criterion incorporates the influences of stress triaxiality and strain rate.

To capture the influence of stress triaxiality, tensile tests were performed on notched specimens in addition to the standard smooth specimen tests. As illustrated in Figure 4.18, the geometry was adapted from previous tests by adding a notch with 2 mm radius. This additional test provides a distinct loading condition alongside different stress and strain states, which is essential for the subsequent calibration of the fracture model.

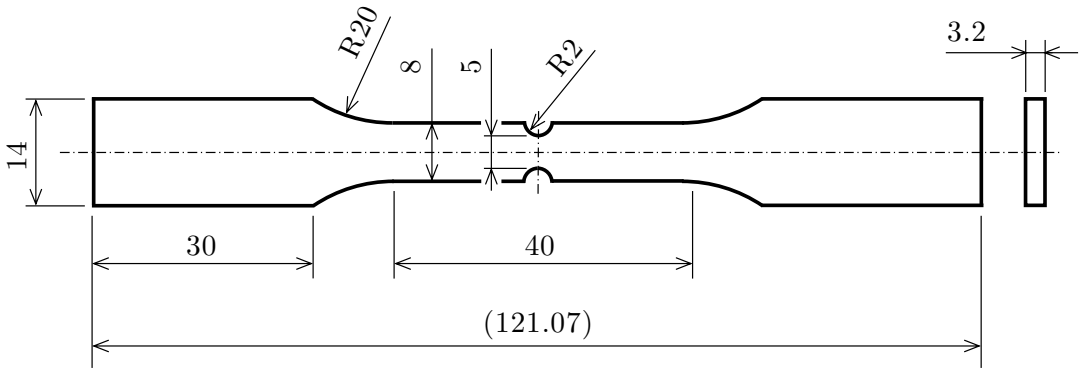



Figure 4.18: Geometry of the notched specimen used for experimental tensile test

Similar to the smooth specimen, the experimental test was replicated using numerical simulation in LS-PrePost software. The entire setup was adopted from the preceding simulation, including the element type, global mesh size, and the previously calibrated multilinear stress–strain curve, which served as the input for the multilinear plastic hardening model. Figure 4.19 illustrates the geometry and boundary conditions used, where only a quarter of the specimen was modeled by exploiting symmetry.

To check the validity of the performed numerical simulation, the obtained reaction force–displacement dependency was compared to the experiment averaged from two tests, shown in Figure 4.20. The relatively large element size resulted in an even more visible error which can be explained by the inability of such elements to sufficiently describe the added notch and changing geometry throughout full simulation time. Furthermore, the variation in material properties between smooth and notched specimens should have also been considered.

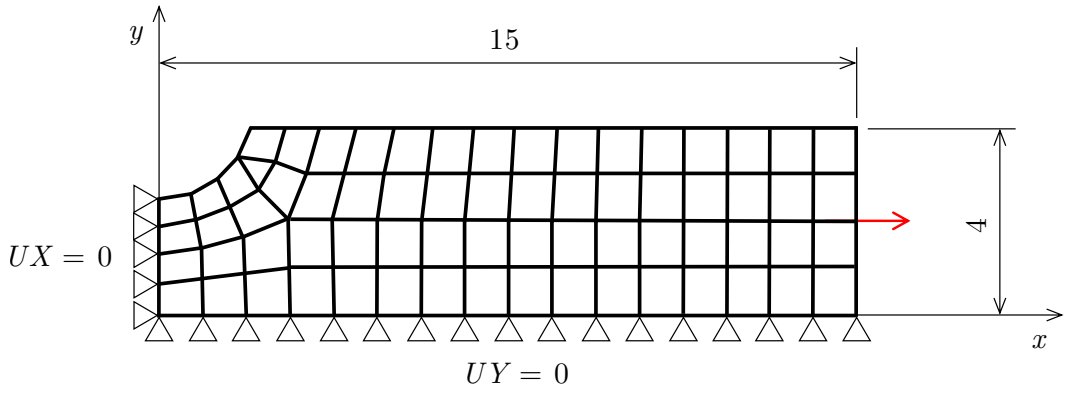



Figure 4.19: Finite element mesh and boundary conditions used in the tensile test simulation of the notched specimen

Despite these factors, the deviation between the computational model and the experiment was sufficiently small (not exceeding 10 %). Consequently, the failure criteria can be calibrated using the values of stress triaxiality and equivalent plastic strain derived from the numerical simulation, as it is impossible to obtain these parameters directly from experiments.

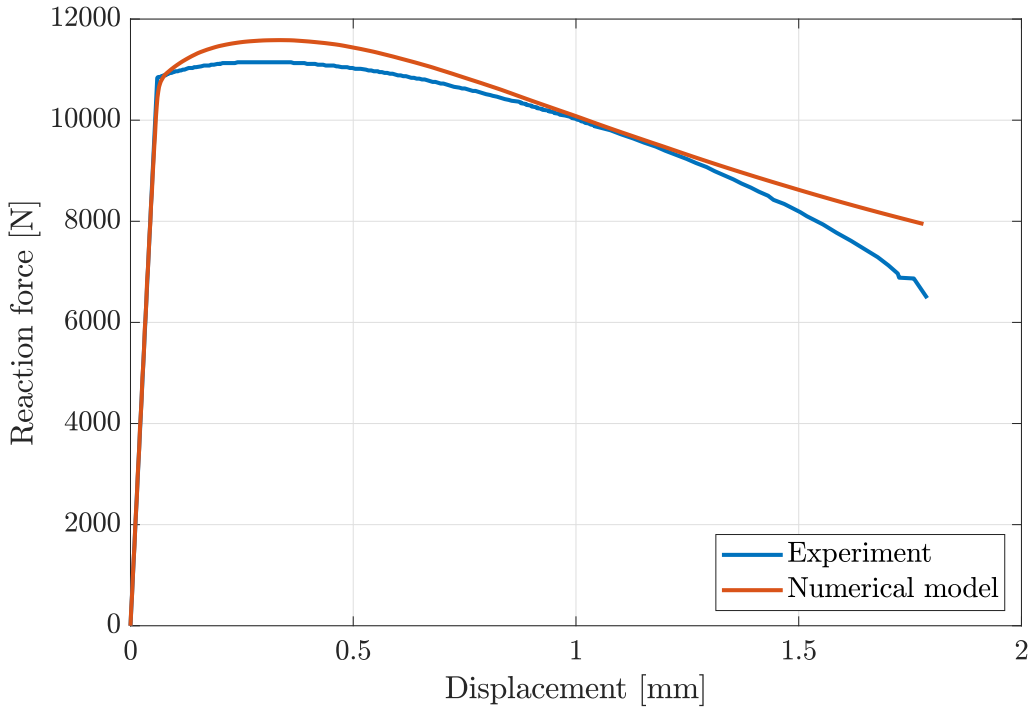



Figure 4.20: Comparison of reaction force–displacement dependencies for the notched specimen

Both stress triaxiality and fracture strain quantities were extracted from the center of the specimens. This approach is consistent with the nature of ductile fracture, which typically initiates at the center of the cross-sectional area for this type of specimen geometry and loading condition. Moreover, both quantities reached their extreme values at the center, confirming this assumption. Due to the fact that the stress triaxiality varies during the simulation, an average value was computed according to [7]:

$$\eta_{av} = \frac{1}{\bar{\varepsilon}_f} \int_0^{\bar{\varepsilon}_f} \eta(\bar{\varepsilon_p}) \mathrm{d}\bar{\varepsilon_p} \tag{4.8}$$

The resulting values of the average stress triaxiality and the fracture strain, shown in Table 4.3, demonstrate that the notched specimen experiences a higher stress triaxiality value, while fracture occurs at a lower value of equivalent plastic strain compared to the smooth specimen.

Table 4.3: Values of average stress triaxiality and fracture strain obtained from numerical simulations

| | **Average stress triaxiality** [–] | **Fracture strain** [–] |
|---|---|---|
| *Smooth specimen* | 0.388 | 0.892 |
| *Notched specimen* | 0.534 | 0.694 |

To obtain the parameters $D_1$, $D_2$ and $D_3$ of the Johnson–Cook fracture model, the dependencies of equivalent plastic strain on stress triaxiality from both tests must be fitted by the function within the first set of brackets given in Equation 3.8 which is shown in Figure 4.21. This fracture model requires at least three various material tests to sufficiently approximate the three-parameter function. As a result of performing only two tensile tests, the coefficient $D_1$ responsible for shifting the curve along the vertical axis was set to zero. It should be noted that obtaining more experimental tests is beneficial for a more comprehensive understanding of the material behavior across a wider range of stress triaxiality values.

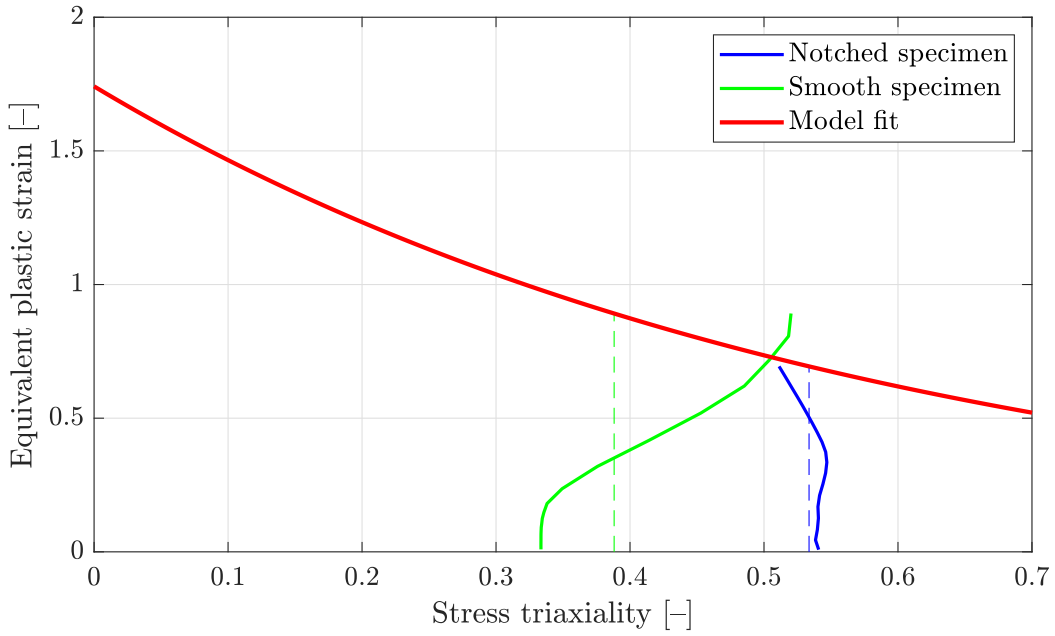



Figure 4.21: Dependencies of fracture strain on stress triaxiality approximated by Johnson–Cook failure model function

The parameter $D_4$, which accounts for the strain rate effect (the second bracket of Equation 3.8), was derived from dynamic experimental tensile tests. As shown in Figure 4.17, there is a visible difference in displacement to fracture between static and dynamic conditions.

After repeating the previously described process of obtaining the dependency of stress triaxiality on the fracture strain (shown in Figure 4.22), the coefficient $D_4$ was determined using Equation 3.8. In this step, the second term of the equation was incorporated by defining the reference strain rate as the quasi-static value ($\dot{\varepsilon}_{sta}(t) = 5.6 \cdot 10^{-4}$ s$^{-1}$) and utilizing the dynamic plastic strain rate, which is three orders of magnitude higher ($\dot{\varepsilon}_{dyn}(t) = 5.6 \cdot 10^{-1}$ s$^{-1}$). The $D_4$ coefficient is then calculated according to:

$$D_4 = \frac{\varepsilon_f^{dyn}}{\left(D_1 + D_2 \exp\left(D_3 \eta_{av}^{dyn}\right)\right) \ln \frac{\dot{\varepsilon}_{dyn}}{\dot{\varepsilon}_{sta}}} - \frac{1}{\ln \frac{\dot{\varepsilon}_{dyn}}{\dot{\varepsilon}_{sta}}} \tag{4.9}$$

The resulting values of average stress triaxiality ($\eta_{av}^{dyn}$) and fracture strain ($\varepsilon_f^{dyn}$) obtained from the dynamic numerical simulation are:

$$\eta_{av}^{dyn} = 0.378 \tag{4.10}$$

$$\varepsilon_f^{dyn} = 0.929 \tag{4.11}$$

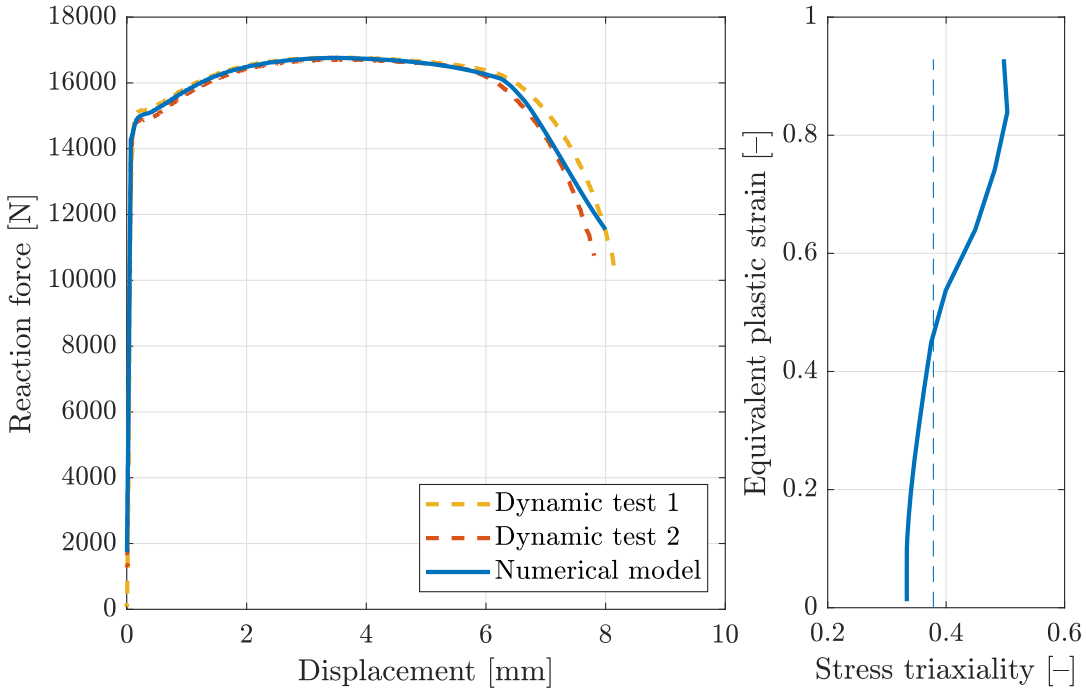



Figure 4.22: Dependency of stress triaxiality on equivalent plastic strain for dynamic test (right side) obtained from calibrated numerical model (left side)

Table 4.4 presents all calibrated material parameters for the Johnson–Cook failure model, which were determined using nonlinear least-squares regression in MATLAB's Curve Fitting Toolbox. The third term of the model (see Equation 3.8), which accounts for thermal softening, was neglected due to the absence of experimental data at elevated temperatures. Consequently, the coefficient $D_5$ was set to zero.

Table 4.4: Calibrated coefficients of Johnson–Cook failure model

| $D_1$ [–] | $D_2$ [–] | $D_3$ [–] | $D_4$ [–] | $D_5$ [–] |
|---|---|---|---|---|
| 0 | 1.7414 | –1.7245 | 0.0034 | 0 |

For this purpose, the material model `*MAT_TABULATED_JOHNSON_COOK (*MAT 224)` was selected for this study. This model enables the use of tabulated input of the plastic hardening curve (variable `LCK1`), the dependence of fracture strain on stress triaxiality (variable `LCF`), and a load curve defining the scale factor for fracture strain as a function of the plastic strain rate (variable `LCG`). The variable `LCI` defines fracture strain scale factor as a function of element size. This variable was implemented due to the unwanted element deletion around bonded contacts which represented the welded joints. Since the material model was calibrated for the refined mesh around the contact point, the arising element failures in the coarser mesh around welded joints were neglected. This was addressed

by increasing the scale factor for the element sizes larger than what the material model was calibrated for, to suppress failure in areas that were not studied in this thesis. Used dependencies (see Figure 4.23) were computed using the previously calibrated material parameters shown in Table 4.4.

It should be noted that the dependency of the fracture strain on the stress triaxiality (variable `LCF` in Figure 4.23) is rotated around the vertical axis, unlike in Figure 4.21. This is due to the fact, that the material model `*MAT 224` defines stress triaxiality as $\eta = p/\overline{\sigma}$, where $p$ is the hydrostatic stress, which is defined as $p = -\sigma_m$.

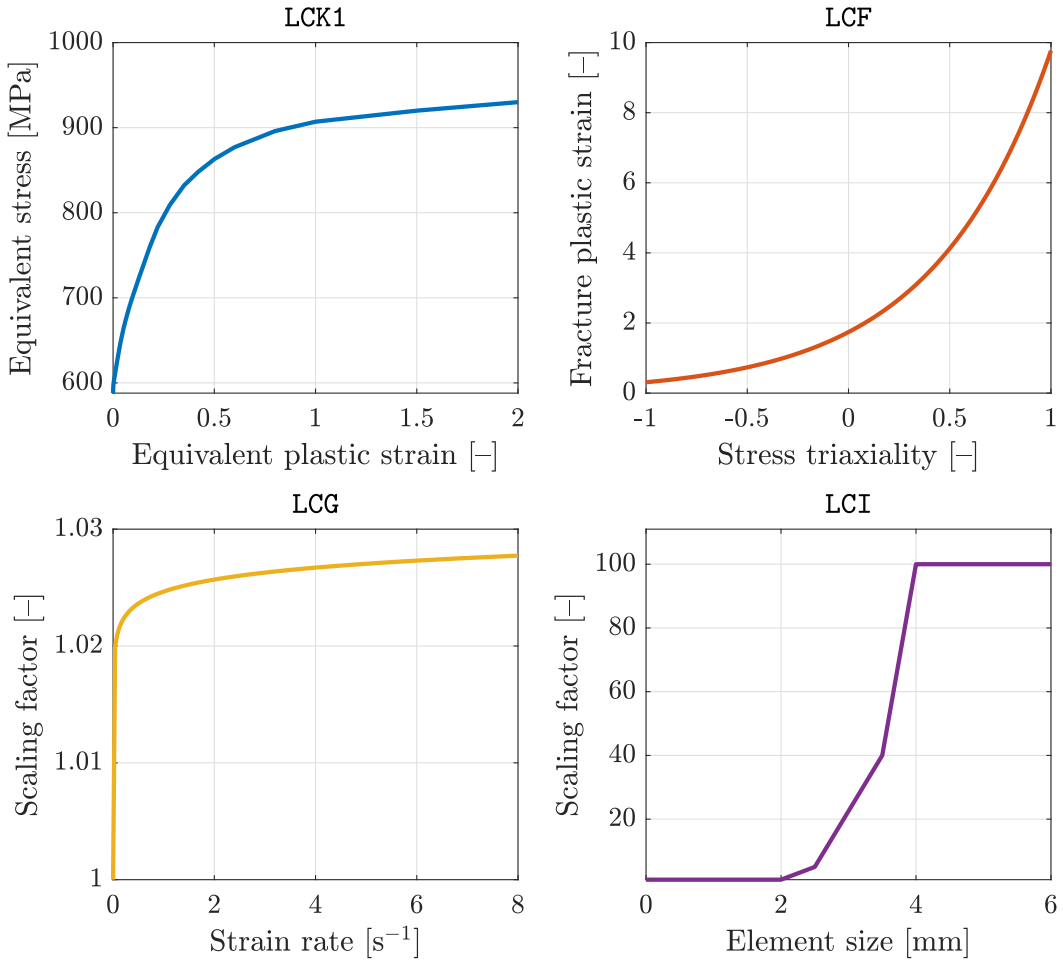



Figure 4.23: Dependencies used is the tabulated Johnson–Cook material model

All material parameters used for the `*MAT_TABULATED_JOHNSON_COOK (*MAT 224)` material model are listed in Table 4.5, where $\mu$ is the Poisson's ratio. Young's modulus as well as Poisson's ratio were calculated from the linear part of the experimental tensile test of the smooth specimen (Figure 4.15). To exclude the temperature effect, the value of specific heat `CP` was set to 1 and the variable `LCKT` (quasi-static dependencies of equivalent stress versus equivalent plastic strain for elevated temperatures) was set to 0, which deactivated the temperature dependent scaling.

Table 4.5: Input parameters for the tabulated Johnson–Cook material model

| $\boldsymbol{E}$ [GPa] | $\boldsymbol{\rho}$ [kg/m$^3$] | $\boldsymbol{\mu}$ [–] |
|---|---|---|
| 229.6 | 7850 | 0.3 |

Due to a lack of available material data for the remaining parts of the suspension assembly, a linear elastic material model `*MAT_ELASTIC (*MAT 001)` was assigned to all deformable parts with same input parameters as in Table 4.5. Conversely, the obstacle and the four auxiliary bodies (displayed in Figure 4.9) were modeled as discrete rigid bodies with assigned material `*MAT_RIGID (*MAT 020)` with identical parameters.

As stated before, a complete listing along with detailed explanation of all material models available for LS-DYNA simulations are provided in **LS-DYNA Keyword User's Manual, Volume II, Material Models** [2].

To ensure the reproducibility and transparency of the simulations, Appendix A provides a comprehensive list of all used LS-DYNA keywords, including one representative example of the parameter settings.

# 5 RESULTS AND DISCUSSION

This chapter provides a detailed comparison of various impact scenarios modeled in the previous chapter to identify the conditions most likely to lead to crack initiation in the axle's torsion beam. Initially, the thesis evaluates the influence of obstacle geometry, impact velocity, and vertical position on the mechanical response of the axle. Subsequently, the material model comparative study is introduced, comparing the Johnson–Cook model calibrated specifically for the purposes of this research against a similar model found in another study. Finally, additional experiment was performed to validate the accuracy of the computational model.

## 5.1 Analysis of impact scenarios

This section is dedicated to comparing impact scenarios constructed in the previous chapter. The section is divided into several parts, each of which evaluates the influence of different phenomena. The thesis compares three obstacle geometries, three impact velocity magnitudes, and two vertical positions of the obstacle to draw a representative conclusion under which operating conditions a potential crack will initiate.

### 5.1.1 Influence of obstacle geometry

To demonstrate the influence of the obstacle geometry on the axle's structural integrity and to accurately compare all three distinct obstacle shapes, the velocity magnitude of 50 km/h and the higher vertical placement were chosen, as this specific setup offers the most visible differences among all simulated impact scenarios.

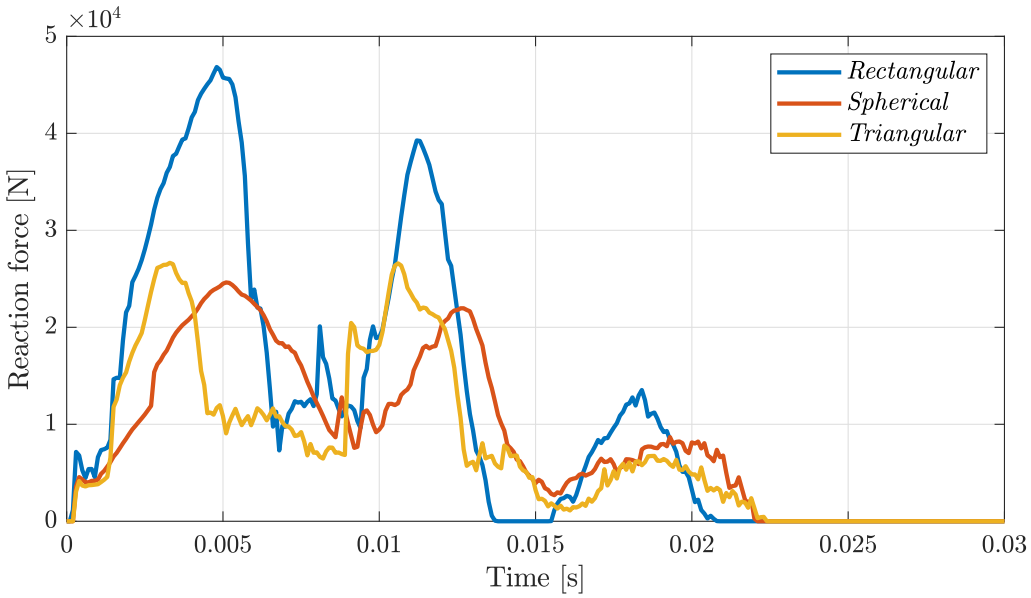



Figure 5.1: Resultant contact force (RCFORCE) comparison for analyzed obstacle geometries at 50 km/h

As shown in Figure 5.1, the rectangular obstacle generates the highest peak reaction force (RCFORCE), which corresponds to the largest contact area during the initial stages of the impact being deformed without reaching the fracture strain. Conversely, the spherical and the triangular obstacles experience similar reaction force values over the simulation time (maximum around 25 kN) due to the much smaller initial contact area. The second peak in the reaction force indicates the obstacle traveling through the axle C-shaped torsion beam profile and hitting the latter side of the axle.

This is supported by Figure 5.2, which depicts the velocity of the moving axle as a function of time. The highest decline in velocity magnitude resulted from the rectangular obstacle, which corresponds to the highest peak in the impact reaction force. The spherical and the triangular obstacles provide less structural resistance to the moving mass, by either allowing the axle to gradually deform (spherical) or almost instantly exceeding the fracture strain, resulting in element deletion and the structural weakening.

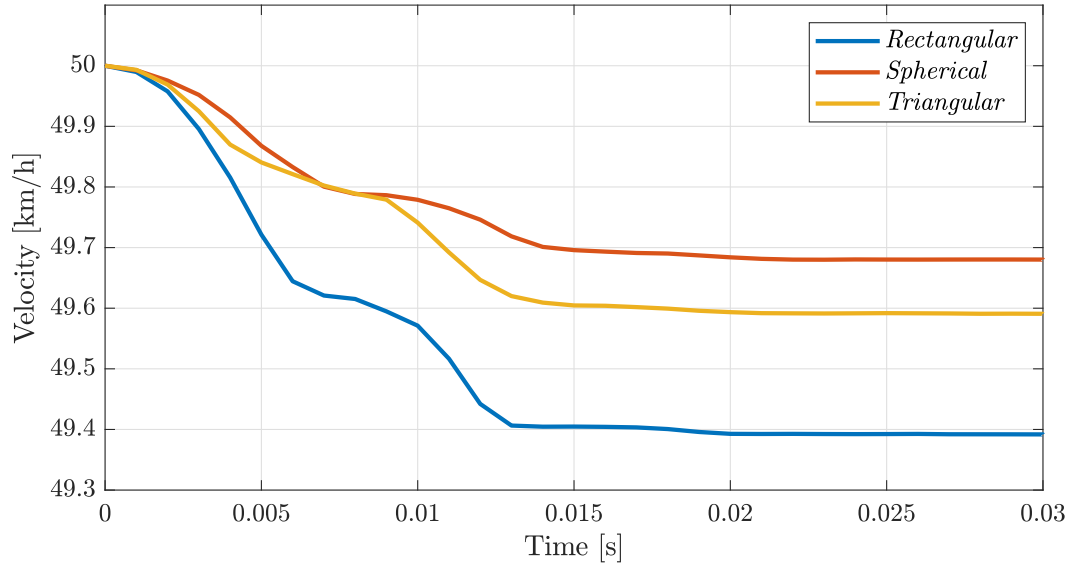



Figure 5.2: Comparison of vehicle velocity reduction during impact for all modeled obstacle geometries

Figure 5.3 displays the deformed shapes of all three impact scenarios with the damage parameter values shown around the contact point. It is visible from the comparison that the triangular obstacle is the most critical option as it creates a very high plastic strain gradient. Consequently, the failure plastic strain is reached almost instantly, resulting in the largest initiated fracture.

The spherical obstacle, as opposed to the triangular one, allows for the smoothest deformation due to the continuous growth of the contact area. As a result, the damage parameter stays well under the critical values with no evidence of crack initiation.

The rectangular obstacle acts as a middle ground between the triangular and the spherical obstacles in terms of the crack initiation. While experiencing the highest global reaction

force and energy dissipation, by distributing the load across an entire flat contact area, the axle is exposed to lower equivalent plastic strain. The crack occurs only at the front of the axle as opposed to the triangular obstacle, which reached the fracture strain also at the other side.

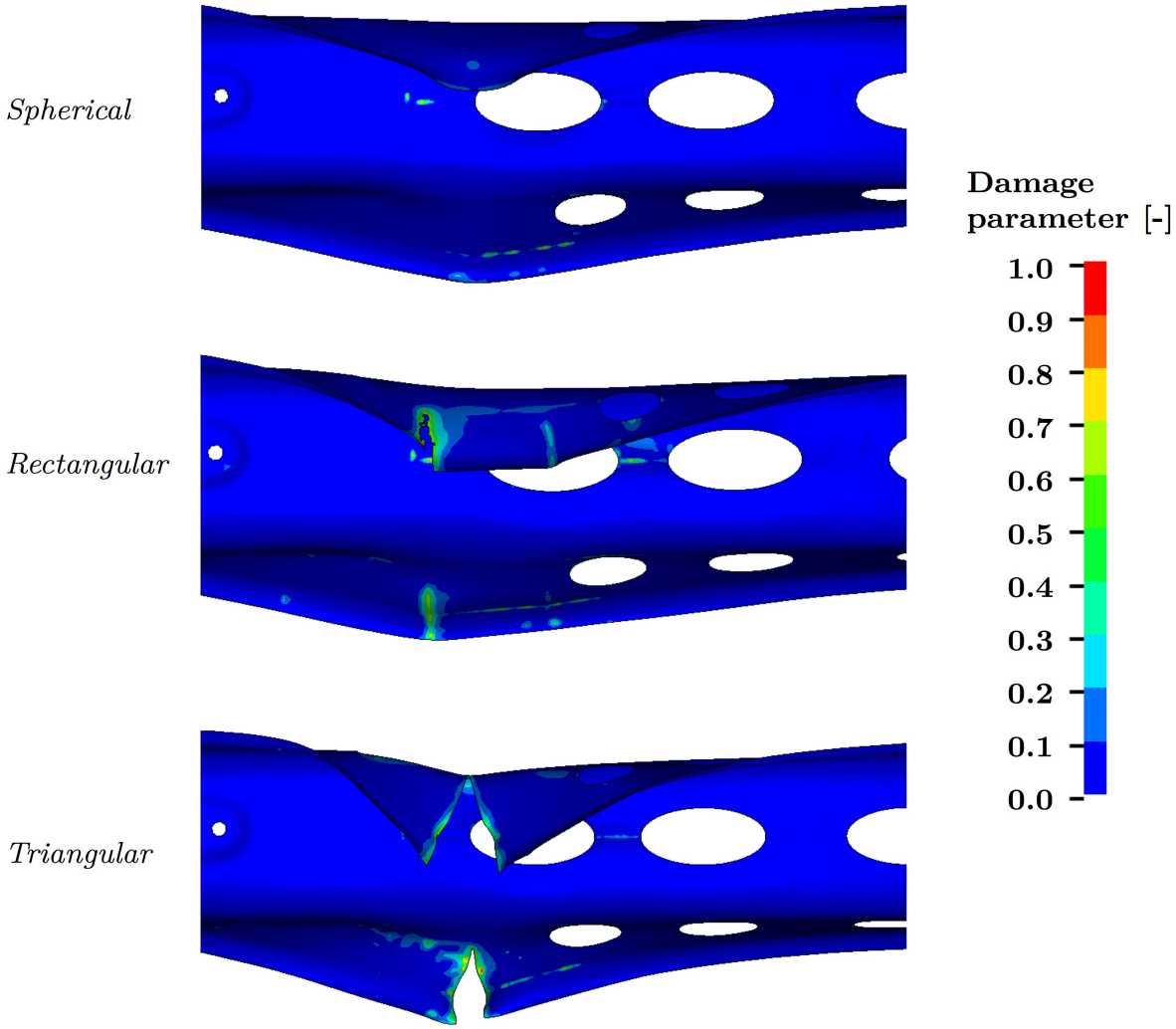



Figure 5.3: Distribution of the damage parameter after impact at 50 km/h for all modeled obstacle geometries

It should be noted that the trends observed in this geometric comparison remain consistent across all tested initial velocities and vertical positions. The 50 km/h configuration was selected as a representative baseline to avoid the influence of the extreme kinematic conditions associated with the 90 km/h impacts. Nevertheless, the relative performance and ranking of the three obstacle geometries remains unchanged across all other modeled configurations.

### 5.1.2 Influence of impact velocity

This subsection examines the influence of various initial velocity magnitudes of the moving suspension colliding with an immovable obstacle. Three distinct velocity values were modeled: **20 km/h**, **50 km/h**, and **90 km/h**. To make the scenarios comparable, the triangular obstacle was utilized in the higher vertical position, as was identified in the previous subsection as being the most critical configuration.

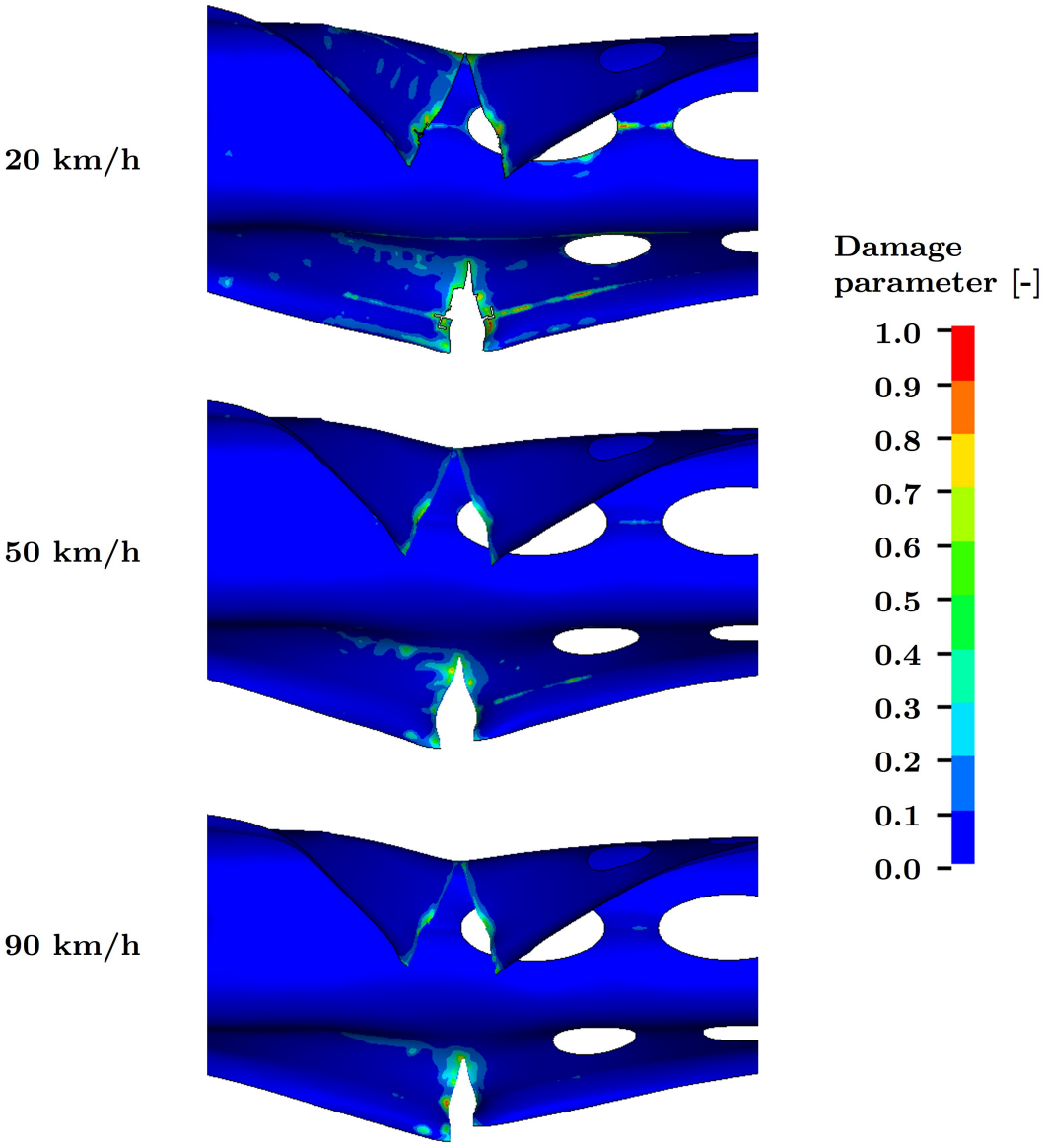



Figure 5.4: Distribution of the damage parameter after impact to the triangular obstacle at all initial velocity magnitudes

Figure 5.4 shows the distribution of the damage parameter values around the contact point right after the impact at all initial velocities. As it is depicted in the figure, the impact resulted in a crack initiation on both sides of the torsion profile for all modeled scenarios. This was caused by the large initial kinetic energy even at the lowest initial velocity due

to the high total mass of the model (≈ 1700 kg) along with a minimal initial contact area of the triangular obstacle resulting in a highly localized load. The other important observation from Figure 5.4 is that the higher the velocity magnitude the smaller the plasticized zone around the fracture. At lower velocities the equivalent plastic strain is disturbed on larger area before the fracture occurs. As opposed to the velocity of 90 km/h where the inertia of the model reduces the distribution of the energy to the surrounding structure making the damage much more concentrated.

The structural response of the three simulated initial velocities is depicted in Figure 5.5, which displays a percentage reduction of each initial velocity averaged across all simulated scenarios i.e., three obstacle geometries in two vertical positions.

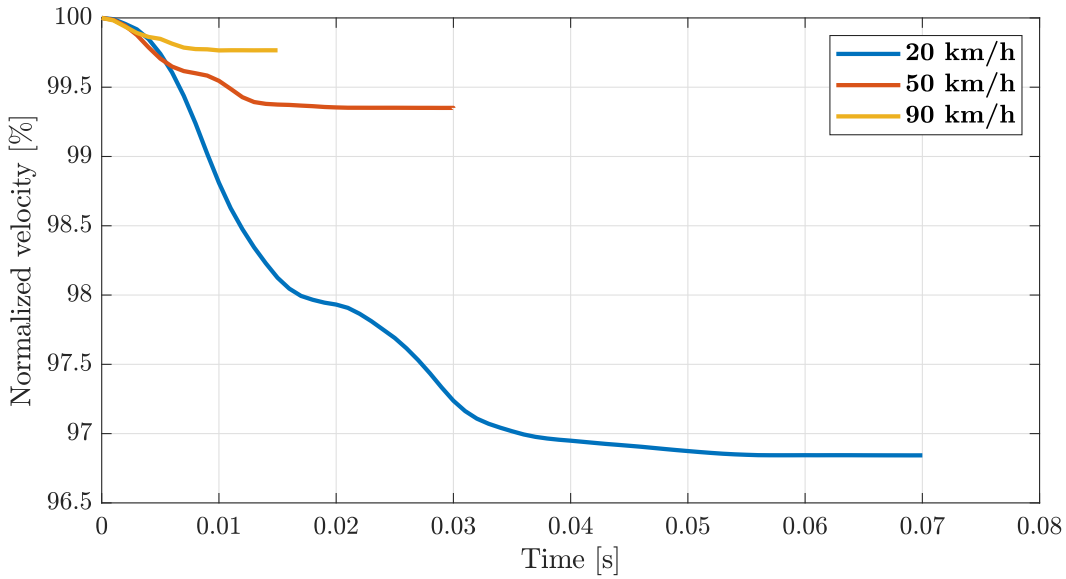



Figure 5.5: Comparison of average relative velocity reduction across the analyzed velocity range for all simulated scenarios

This observation confirms the findings depicted in Figure 5.4, where the damage at the initial velocity of 20 km/h is more widely distributed across the axle body. As it is shown in Figure 5.5, at this initial velocity, the average percentage reduction is the largest (≈ **3.16 %**) meaning that the largest amount of kinetic energy of the model is transformed into deformation energy within the axle material. Conversely, at 90 km/h the average velocity reduction is a negligible **0.23 %**.

### 5.1.3 Influence of vertical position

The vertical position of the impact point is crucial in the structural response of the torsion beam directly impacting the size of the damaged area and potential fracture. As was previously stated, the thesis compares two vertical positions of the obstacle with a difference of 25 mm (see Figure 4.6). The higher configuration represents a worse scenario impacting a larger area of the axle, whereas the lower position simulates a less dangerous situation. To keep the comparison representative, the velocity magnitude of 50 km/h was chosen to find out the influence the vertical position has on potential fracture initiation and material response.

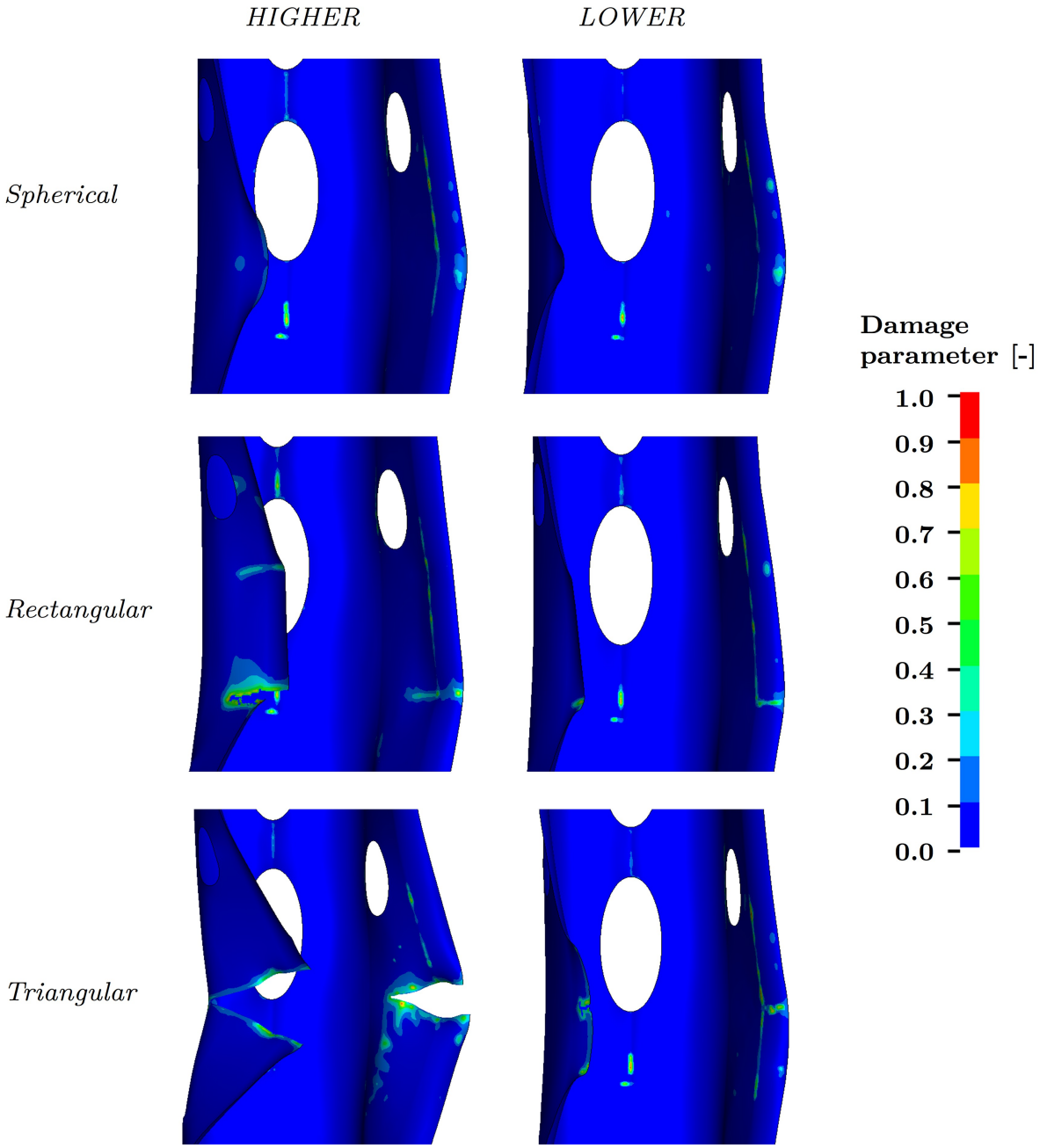



Figure 5.6: Comparison of a damage parameter distribution at different vertical position of the obstacle for initial velocity of 50 km/h

As it is shown in Figure 5.6, the lower vertical position significantly reduces the damage parameter and the deformation of the axle. This is caused by the fact that the obstacle position allows the axle to deform without reaching the fracture strain as the structural resistance of the material is reduced. For example, the lower position of the obstacle significantly reduced the initiated fracture when using the triangular obstacle (the size of the initiated crack is much smaller and it is formed only at the front side of the torsion profile) and completely prevented the initiation when using the rectangular obstacle.

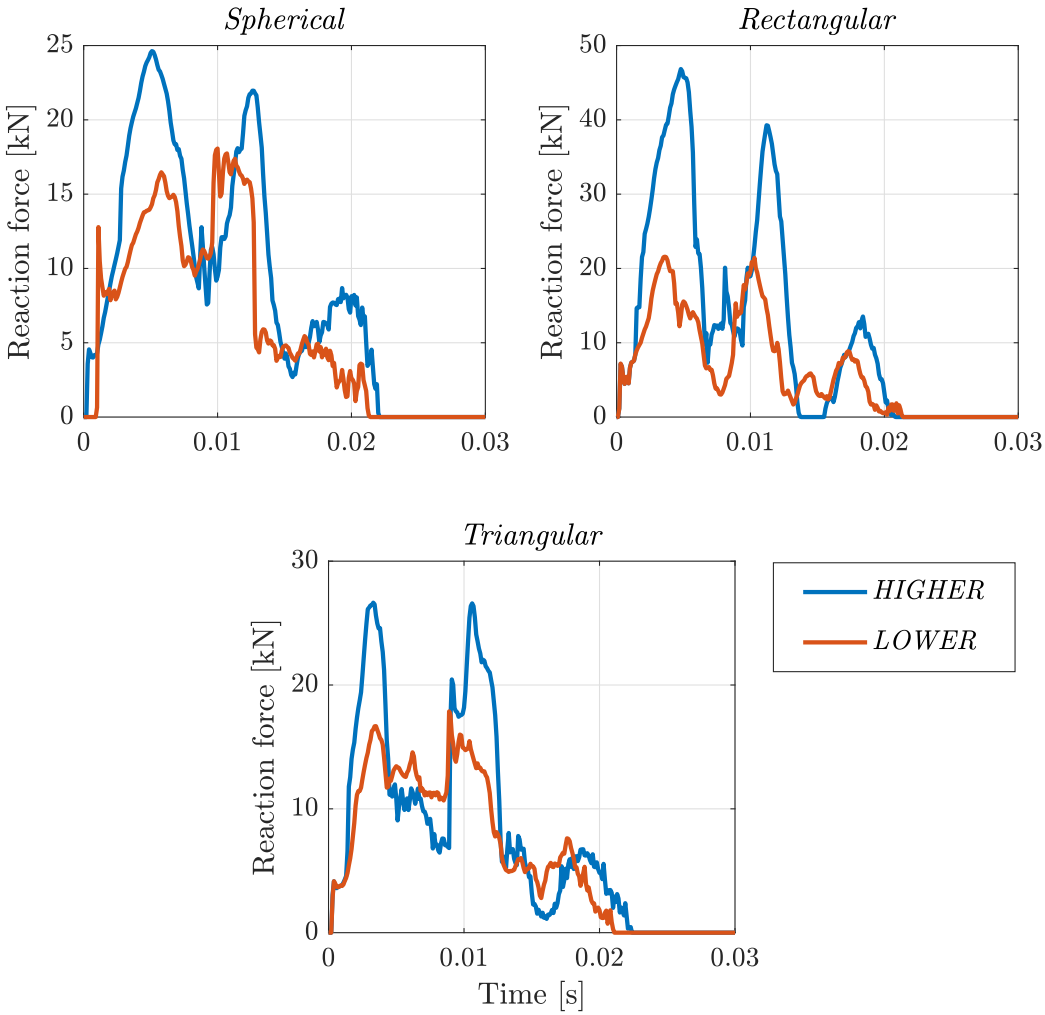



Figure 5.7: Comparison of the reaction force for both vertical positions for all obstacle geometries at 50 km/h

Figure 5.7 compares the reaction force of both vertical positions of each of the used obstacles. The lower position visibly reduces the loading force on the axle body in all simulated scenarios by approximately 38 % and directly influencing the amount of kinetic energy of the model dissipated within the material as internal energy, thereby leading to plastic deformation.

### 5.1.4 Comparative summary of simulated impact scenarios

To conclude the study of various impact scenarios of the rear torsion beam axle, this subsection compares all 18 simulations to determine a sufficiently accurate threshold at which the integrity of the axle is compromised.

Table 5.1 provides a summary of each combination of initial velocity magnitude, obstacle geometry, and vertical position regarding potential fracture initiation.

Table 5.1: Comparison of crack initiation in all simulated impact scenarios

| | | **20 km/h** | **50 km/h** | **90 km/h** |
|---|---|---|---|---|
| | *Triangular* | YES | YES | YES |
| *HIGHER* | *Rectangular* | YES | YES | YES |
| | *Spherical* | NO | NO | NO |
| | *Triangular* | YES | YES | YES |
| *LOWER* | *Rectangular* | YES | NO | NO |
| | *Spherical* | NO | NO | NO |

The table confirms that the triangular obstacle represents the most critical geometric configuration among all evaluated shapes. Regardless of the initial velocity magnitude or the vertical position of the obstacle, the fracture was always initiated. Conversely, the spherical obstacle did not weaken the axle structure even at the most aggressive configuration (initial velocity of 90 km/h at the higher position). This phenomenon is caused by the ability of the spherical obstacle to distribute the load more evenly, thereby allowing the axle to gradually deform as the obstacle is in contact with the axle.

The comparative analysis suggests that the vertical position and the geometry of the obstacle have a more significant influence on the structural response and potential crack initiation than the velocity magnitude of the moving vehicle. This is evidenced by the fact that a fracture occurred even at the velocity of 20 km/h when using the triangular and rectangular obstacles. In contrast, employing a less aggressive geometry in a safer vertical position proved to be a more reliable strategy for maintaining the structural integrity of the axle as it allows for more effective energy dissipation through stable plastic deformation of the more compliant regions of the torsion beam rather than localized loading, which could potentially lead to the material separation.

## 5.2 Material model comparative study

This section is dedicated to a material model comparison for conducting a material model comparative study. The calibrated and tabulated Johnson–Cook model (`MAT 224`) developed from experimental testing for this thesis is compared to the analytical Johnson–Cook model (`MAT 015`) taken from the doctoral thesis written by Ahmad in 2012 [1] and developed for ballistic simulations of a blast loading of multi-layered steel plates. Both material calibrations were conducted on similar high-strength, low-alloyed, hot-rolled steel, which is widely used in the automotive industry.

Table 5.2 includes all input parameters used for the Ahmad material model where $c$ is the specific heat value.

Table 5.2: Input parameters for the Ahmad Johnson–Cook material model [1]

| $E$ [GPa] | $\rho$ [kg/m$^3$] | $\mu$ [–] | $c$ [J/kg.K] |
|---|---|---|---|
| 210 | 7850 | 0.33 | 452 |

| $A$ [MPa] | $B$ [MPa] | $n$ [–] | $C$ [–] | $m$ [–] |
|---|---|---|---|---|
| 560 | 757 | 0.75 | 0.014 | 1 |

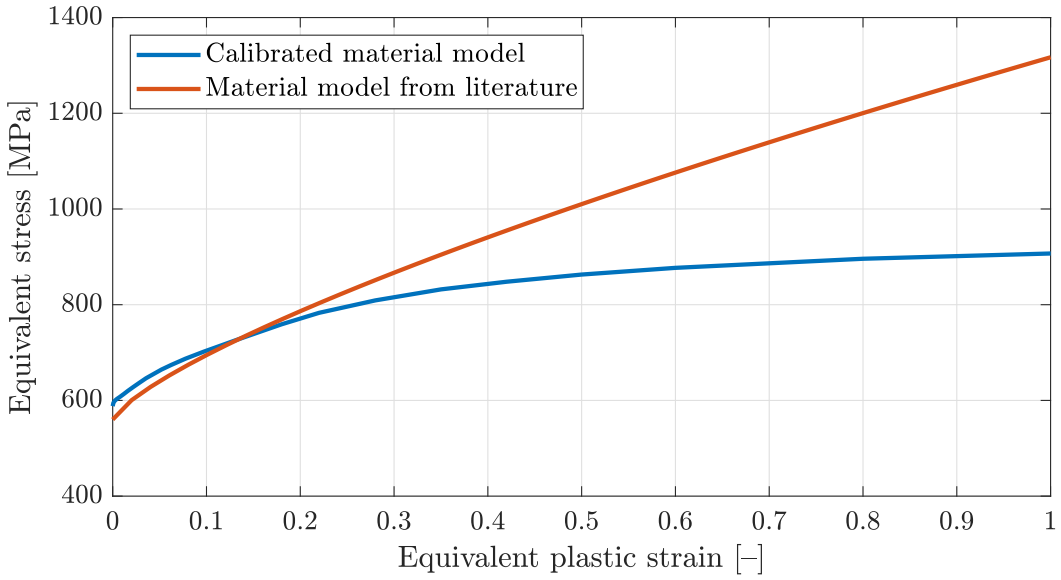



Figure 5.8: Hardening curve comparison between the calibrated and tabulated Johnson–Cook model and the Johnson–Cook model from [1]

Figure 5.8 compares the hardening curves (equivalent stress as a function of equivalent plastic strain) for both material models. The difference is caused by the mathematical description of the hardening behavior of each model. While the model constructed for the purposes of this thesis utilizes the tabulated input, the Ahmad material uses the power--law hardening model (see Equation 3.7). Other reasons causing the visible deviation could be differences in computational models used for the calibration or microstructure. In the Ahmad thesis [1], the simulation was performed using axi-symmetric modeling with element sizes of 0.2 and 0.4 mm.

Since the Johnson–Cook model of Ahmad [1] lacks a failure criterion for element deletion, the benchmark configuration selected for this comparison is the spherical obstacle with the initial velocity magnitude of 50 km/h, because it does not initiate material deletion and stays within the elastic–plastic regime.

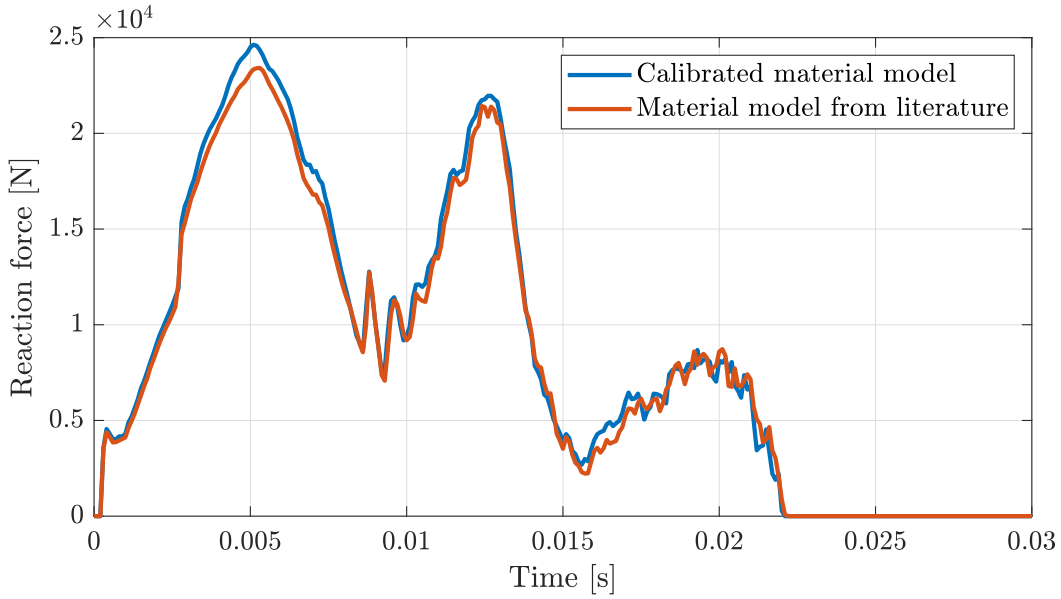



Figure 5.9: Reaction force comparison between the calibrated and tabulated Johnson–Cook model and the Johnson–Cook model from [1]

Figure 5.9 compares the reaction force values over the simulation duration between the obstacle and the torsion beam. The calibrated and tabulated Johnson–Cook model exhibits a slightly greater force response value due to its slightly higher yield stress (588 MPa vs. 560 MPa). This is further quantified in the internal energy history curve depicted in Figure 5.10 where the calibrated model absorbs approximately 12 % more of the kinetic energy of the moving axle than does the model of Ahmad [1].

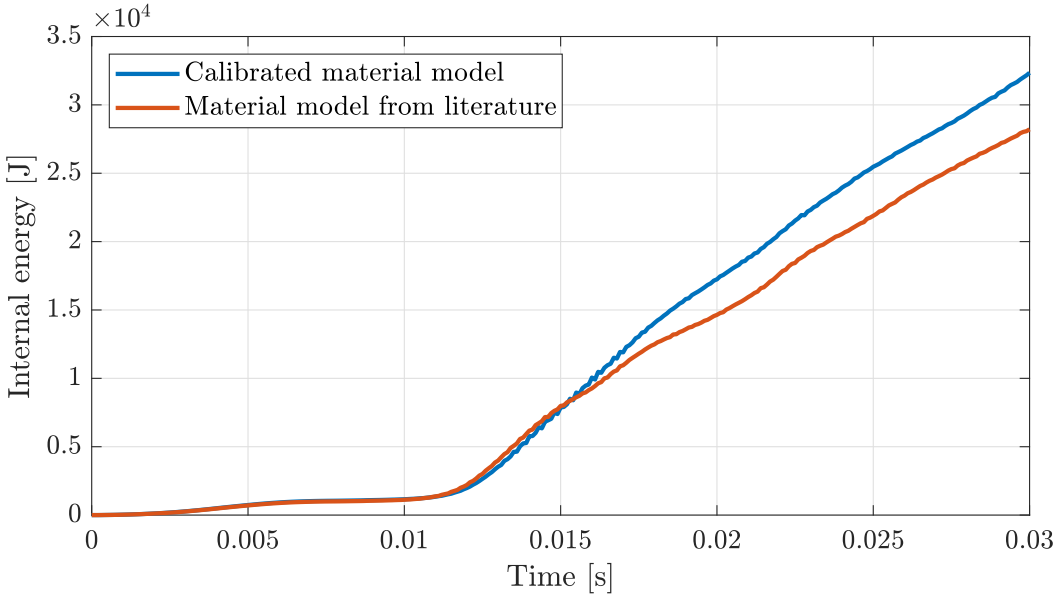



Figure 5.10: Comparison of internal energy dissipation between the calibrated Tabulated Johnson–Cook model and the Johnson–Cook model from [1]

As it is depicted in comparison of equivalent strain distributions in Figure 5.11, a notable difference occurred. The calibrated material model underwent a larger plastic deformation, which is visible on both sides of the torsion beam due to the softer slope of the plastic hardening curve at higher equivalent plastic strain values.

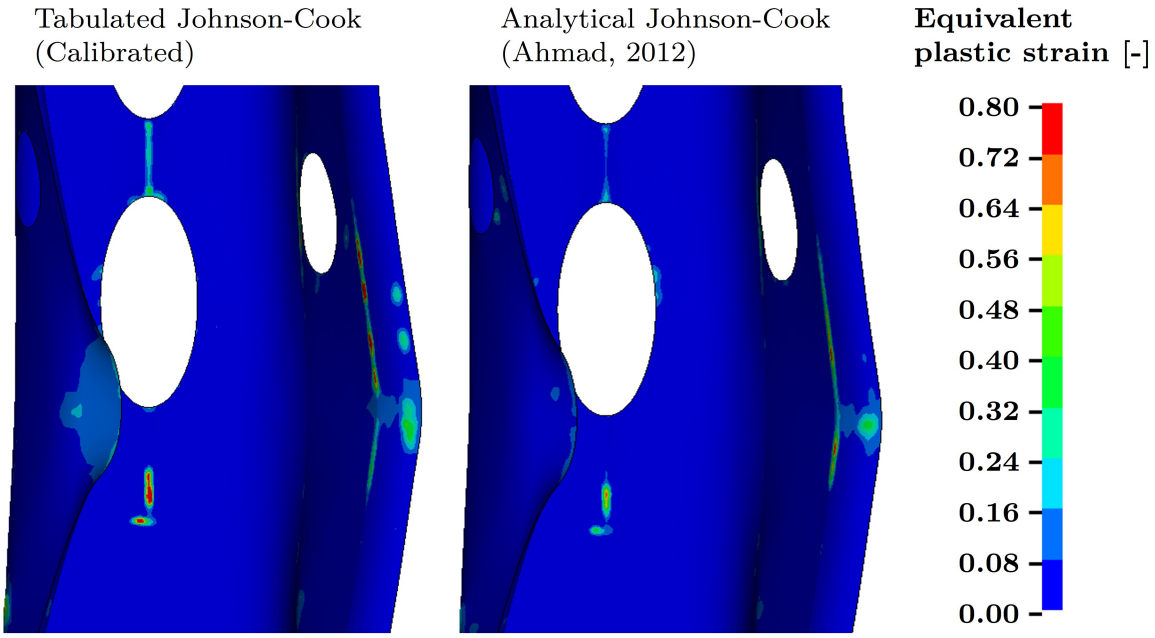



Figure 5.11: Comparison of equivalent plastic strain distributions for both studied material models

## 5.3 Validation with impact experiment

This section contains a validation of the constructed computational model including calibrated Johnson–Cook material model (`*MAT_TABULATED_JOHNSON_COOK`) against a controlled experiment, which was carried out externally not by the student, simulating a real impact.

The experimental setup, which is shown in Figure 5.12, involved a rear torsion beam suspension of the same type as the one used in the previous computational simulations, mounted on a custom-built frame built in the Department of Machine Parts and Mechanisms of the Faculty of Mechanical Engineering of the Technical University of Liberec. Consistent with the computational model, the mounting of the suspension reflected the real-world scenario as closely as possible, utilizing the original shock absorbers and springs with correct pretension. To ensure a controlled and safe experimental environment, the impact was performed in an opposite manner compared to the modeled simulations. While the simulations involved a moving torsion beam axle colliding with a stationary rigid obstacle, the physical experiment utilized a hydraulic piston-driven obstacle impacting a fixed axle.

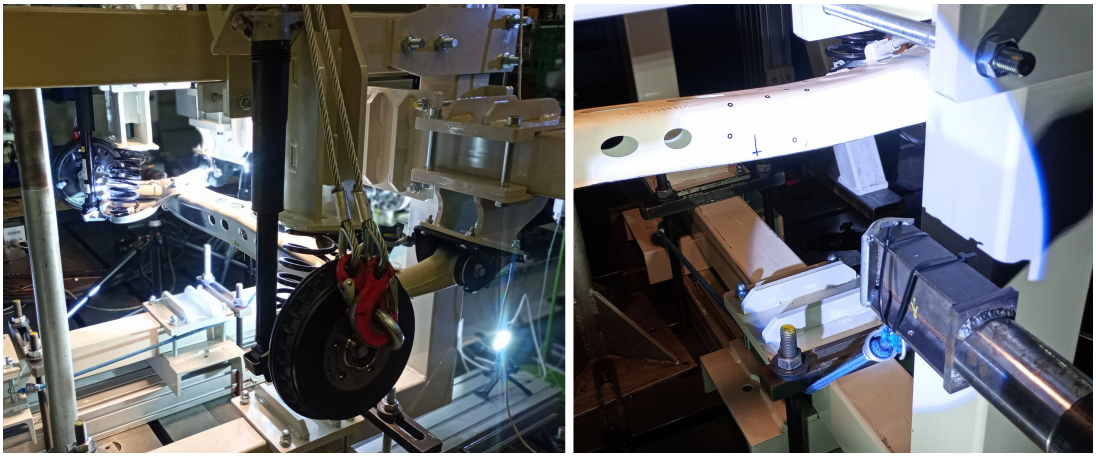


Figure 5.12: Experimental setup for the dynamic impact validation

To make the computational simulation comparable with the experiment, necessary modifications in boundary conditions were required. Restricting all translational DOFs of the solid auxiliary bodies which acts as mounting points for springs and shock absorbers (depicted in Figure 4.9) and the translation in the $x$ axis of both bush housings, the axle faithfully replicated the experimental conditions ensuring a fixed placement of the axle while preserving the ability to rotate around both front bearings. The modification was implemented by adjusting the `CON1` and `CON2` values in the `*MAT_RIGID (*MAT 020)` material keyword settings.

Figure 5.13 depicts the impactor used in the experiment along with its finite element representation. The correct reproduction of the used obstacle is crucial in sufficient comparability of experimental and numerical modeling. Similarly to other obstacles used in

this study, a material model `*MAT_RIGID (*MAT 020)` was used with global mesh element size of 4 mm.

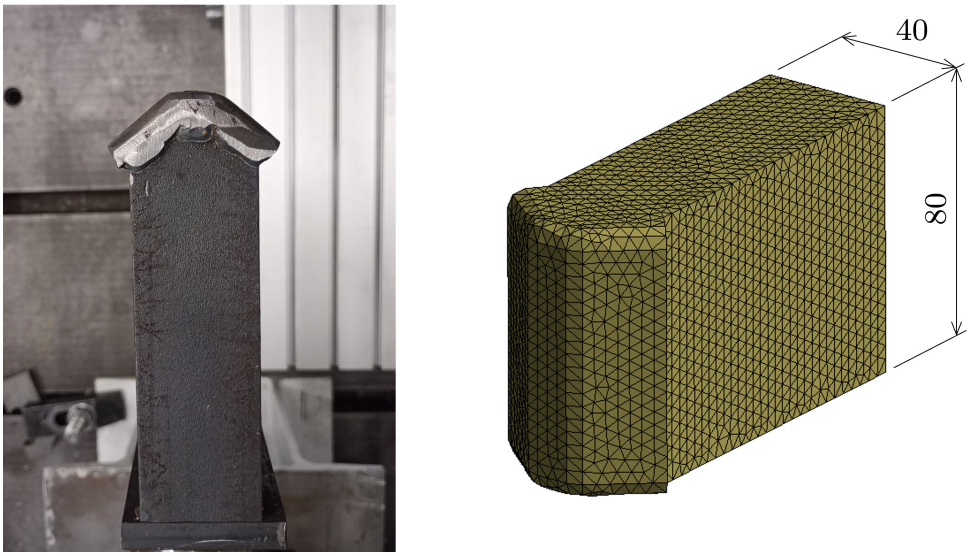



Figure 5.13: Geometry and finite element discretization of the experimental impactor

The experimental data were acquired by a DEWE 5000 at sampling frequency of 20 kHz using five sensors and a high-speed camera recording in sampling frequency of 448.5 Hz.

One of the main limitation of the numerical model was the inability to accurately replicate the inertial properties of the hydraulically driven impactor due to insufficient experimental data. To compensate, the material density of the impactor in the numerical model was adjusted iteratively using a trial-and-error approach, with the objective of matching the maximum value of measured force reaction while maintaining the target impact velocity generated by the hydraulic piston. Since this is one of the main weaknesses of the model, it should be addressed in future studies.

Figure 5.14 depicts comparisons of the impact velocity reduction by the collision and the reaction force curve between the experiment and the numerical simulation. Both comparisons confirm notable differences in energy dissipation capabilities between the experiment and the computational model. Despite ensuring identical initial kinetic energy values by matching the impact velocity magnitudes ($\approx$ 30.5 m/s), the numerical model exhibits a more aggressive deceleration, in contrast to the experiment which takes approximately twice as long to reach zero velocity. Consequently, the reaction force comparison confirms a softer and more compliant behavior of the suspension in the experimental model, as evidenced by the fact that the obstacle remained in contact with the axle for nearly four times as long. The discrepancy in the stiffness of both models is caused by the idealized boundary conditions in the computational model. In reality, the custom-built frame and the hydraulic piston add a non-negligible damping and flexibility to the experiment, which are impossible to capture by fully fixed boundary conditions and rigid obstacle.

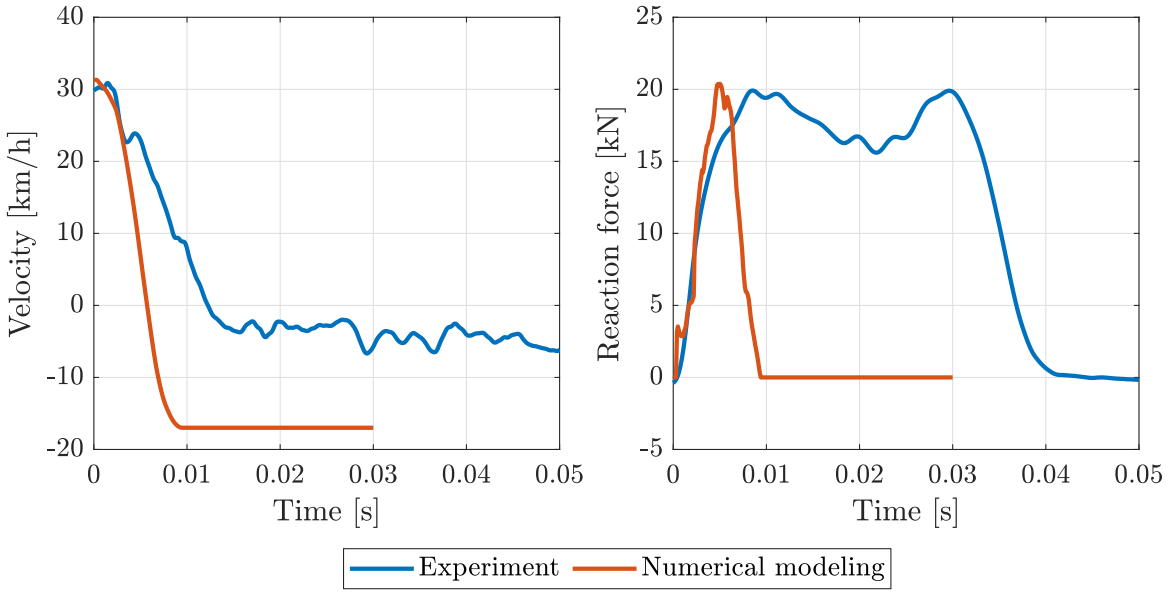



Figure 5.14: Comparisons of velocity reduction curves (on the left) and reaction force profiles between experimental and numerical results

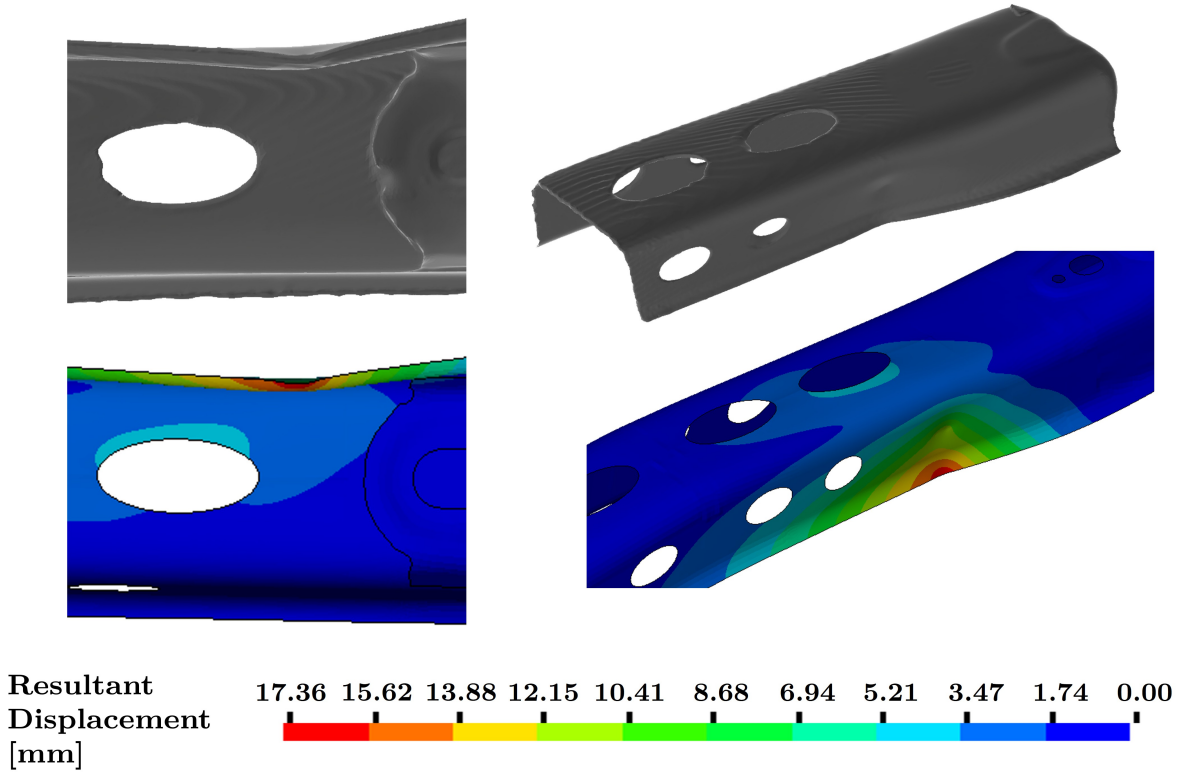



Figure 5.15: Comparison of deformed geometries after the impact between experimental and numerical results

To accurately compare the permanent deformation of the structure after the impact, the axle used in the experiment was scanned and converted into a digital STL surface geometry. Figure 5.15 illustrates the comparison between the scanned specimen and the deformed geometry from simulation, where the two deformed shapes show negligible visual discrepancy. By overlaying the pre- and post-impact scans in SpaceClaim 2025 R2 software, a maximum resultant displacement of approximately 17–18 mm was identified, which correlates well with the numerical simulation results.

In conclusion, although the experiment introduced a notable deviation in the force response and energy dissipation (reflected in the differences in velocity reduction), which was mostly caused by the inability of the numerical model to capture the flexibility and damping of the experimental frame, the high correlation in the deformed geometry proves that the calibrated Johnson–Cook material model is sufficiently capable of capturing the complex material response and reliably predict the potential structural failures.

# 6 CONCLUSION WITH SUGGESTIONS FOR FUTURE STUDIES

The objective of this diploma thesis was to conduct a stress–strain numerical analysis of the rear torsion beam suspension after a contact with a foreign road obstacle. The objective was to study the material response and review a possibility of fracture initiation across a wide range of potential situations differing in vehicle velocity, obstacle geometry, or vertical position of the obstacle.

The first part of the study, presented in Chapter 2, covered an overview of different types of suspension systems used in today's vehicles by describing their features and design flaws. First, the main components of a suspension system were explained, followed by a list of the most commonly used types. Finally, research was conducted into possible damage mechanisms and the contributing situations, which may lead to suspension damage.

In Chapter 3, a theoretical research was carried out. The study included a description of the explicit formulation of the finite element method, covering the basic principles of the formulation and the crucial differences between explicit and implicit approaches, along with their corresponding applications. Subsequently, the theoretical study covered the description of models of plasticity and ductile fracture, with an emphasis on the Johnson–Cook material models.

The practical section began with a comprehensive procedure about the creation of the computational model in Chapter 4, through which the impact scenarios were simulated. The obtained geometry of rear torsion beam suspension was transformed into surface model to reduce computational time. Subsequently, three distinct road obstacle shapes were selected in two vertical placements (as the horizontal placement was predetermined) to cover a wide range of potential impact scenarios and present sufficiently reliable conclusions. The model was constructed to simulate the worst–case scenario regarding the vehicle's loading capacity. Despite obtaining only the torsion axle geometry, the computational model was able to accurately represent the impact conditions by preserving corresponding inertial properties of entire vehicle. This was achieved by accurately assigning the sprung and unsprung masses including implementing nonlinear spring and shock absorber characteristics. Another important criterion for sufficiently assessing potential structural failure is the vehicle impact velocity. The study compared three initial velocity magnitudes (20 km/h, 50 km/h, and 90 km/h) to incorporate a representative range of real-world driving conditions without introducing unnecessary extreme scenarios.

The chapter also provided a detailed calibration of the material models required for the simulations, derived from performed tensile tests. The Johnson–Cook plasticity and failure models were chosen for the torsion beam material due to their ability to account for the influences of stress triaxiality and strain rate, both of which are essential for capturing the structural response under dynamic impact. Due to the visible deviation between the calibrated flow curve and the Johnson–Cook hardening power–law function, the tabulated Johnson–Cook model was selected. This approach enabled the use of tabulated input for

the plastic hardening curve directly, avoiding the need for approximation by a power-law function.

Subsequently, the simulation results, including a model validation, were provided in Chapter 5. First, the chapter examined the influence of the various constructed scenarios. In total, 18 different situations were simulated, differing in three impact velocity magnitudes and three different obstacle geometries at two different vertical placements of the impact. The study showed that the vertical position of the impact and the obstacle geometry have a more significant effect on the structural integrity of the axle than the initial impact velocity of the vehicle. This was proven by the fact that the triangular (the most aggressive) obstacle caused fracture initiation in all simulated scenarios. Conversely, the torsion beam was able to withstand the spherical obstacle (the least aggressive) in all scenarios without reaching the fracture strain.

Second part of the chapter was dedicated to a comparative material study, which compared the previously calibrated and tabulated Johnson–Cook model with a Johnson–Cook model from literature for the same high-strength steel. Since the literature contained only the plasticity model, the comparison was carried out using the spherical obstacle at an impact velocity of 50 km/h. Despite a notable difference in the hardening curves, presented equivalent plastic strain distributions showed only minor differences in local extremes. These were most likely caused by the different meshes used for the calibration of each of the respective models.

The study was concluded with a validation against a controlled experiment, which simulated the impact using a hydraulically driven impactor. Necessary adjustments were implemented to the computational model to match the experimental configuration. Specifically, while the original model featured a moving axle, the validation setup was adjusted to a moving obstacle colliding with a stationary axle. After modifying the inertial properties of the moving impactor to match the impact velocity and maximum value of the reaction force, the simulated deformed geometry showed no significant deviation compared to the experiment. This demonstrates that the model can accurately capture the complex material response and predict potential structural failure, despite a notable deviation in the force response and the energy dissipation caused by the model's inability to incorporate the compliance of the custom-built experimental rig.

### Suggestions for future studies

While the study succeeded in creating a robust computational model, which can effectively predict the material response under a dynamic loading, several suggestions for future improvements have been recognized to enhance the predictive accuracy of the model.

First, the calibration of the failure material model could be improved by incorporating data from additional tensile tests on notched specimens. To accurately calibrate the three-parametric Johnson–Cook failure model used in this thesis, a minimum of three equivalent plastic strain–stress triaxiality dependencies are required. Furthermore, a more comprehensive investigation of the strain rate effect would significantly improve the ability to capture the material behavior during high-speed impacts.

Additionally, a more precise defining of the welded joints would also improve the fidelity of the model. Creating the physical weld geometry or implement heat-affected zones would offer a better understanding of material behavior around the joints, rather than using fixed contacts often associated with unrealistic stress values.

To resolve the observed deviations from the experiment, future work should focus on modeling the entire testing rig and accurately characterizing the inertial and material properties of the impactor. This would allow for more rigorous validation of the numerical model against experimental results, ultimately improving its overall predictive capability.

Finally, to account for manufacturing tolerances and the fact that the material properties found in literature are not deterministic, a stochastic analysis should be performed. Providing a probabilistic view into axle's behavior would ensure the structural safety across a wider range of possible variations.

Despite the listed limitations and areas for improvement, this thesis has successfully established a foundational framework for the computational modeling of a rear torsion beam suspension under impact loading, providing a solid ground for future research.

# BIBLIOGRAPHY

[1] Ahmad, M. S. *Study of Dynamic Behaviour of Multi-Layered Structures Subjected to Blast Loading*. Rondebosch, South Africa, 2012. Doctoral thesis. University of Cape Town, Department of Mechanical Engineering. Blast Impact and Survivability Research Unit (BISRU). Available from: http://hdl.handle.net/11427/10005.

[2] Ansys, Inc.. *LS-DYNA Keyword User's Manual, Volume II, Material Models*. Online. R14. Canonsburg, PA: Ansys, Inc., 2023 [Cited 12. March 2026]. Available from: https://ftp.lstc.com/anonymous/outgoing/web/ls-dyna_manuals/R14/LS-DYNA_Manual_Volume_II_R14.pdf.

[3] Ansys, Inc.. *LS-DYNA Keyword User's Manual, Volume I*. Online. R14. Canonsburg, PA: Ansys, Inc., 2025 [Cited 12. March 2026]. Available from: https://ftp.lstc.com/anonymous/outgoing/web/ls-dyna_manuals/R14/LS-DYNA_Manual_Volume_I_R14.pdf.

[4] Audi AG. *Front suspension - Audi Technology Portal*. Online. 2026. Available from: https://www.audi-technology-portal.de/en/chassis/wheel-suspension-steering/front-suspension. [Cited 5. May 2026].

[5] Belytschko, T., Liu, W. K., Moran, B. and Elkhodary, K. I. *Nonlinear Finite Elements for Continua and Structures*. 2nd ed. Chichester, West Sussex: John Wiley & Sons, Ltd, 2014. ISBN 978-1-118-63270-3.

[6] Blue Strada Tours. *Car Suspension Kinematics Schemes*. Online. 2025. Available from: https://bluestradatours.com/car-suspension-kinematics-schemes/. [Cited 12. November 2025].

[7] Boňkovec, J. *Computational Simulation of Material Cutting Process*. Brno, 2008. Doctoral thesis. Brno University of Technology, Faculty of Mechanical Engineering.

[8] Bridgman, P. W. *Studies in Large Plastic Flow and Fracture*. 1st ed. New York: McGraw-Hill Book Company, Inc., 1952. Metallurgy and Metallurgical Engineering Series.

[9] Dayton, T. *Live Axle*. Online. 2017. Available from: https://www.counterman.com/counter-view-live-axle/. [Cited 16. October 2025].

[10] Dowling, N. E. *Mechanical Behavior of Materials: Engineering Methods for Deformation, Fracture, and Fatigue*. 4th ed. Harlow, Essex: Pearson Education Limited, 2013. ISBN 978-0-273-76455-7.

[11] Goodarzi, A., Lu, Y. and Khajepour, A. *Vehicle Suspension System Technology and Design*. Springer, 2023. Synthesis Lectures on Advances in Automotive Technology. ISBN 978-3-031-21804-0.

[12] Jazar, R. N. *Vehicle Dynamics: Theory and Application*. 2nd ed. New York, NY: Springer, 2014. ISBN 978-1-4614-8544-5.

[13] Johnson, G. R. and Cook, W. H. A constitutive model and data for metals subjected to large strains, high strain rates and high temperatures. In: *Proceedings of the 7th International Symposium on Ballistics*. The Hague, The Netherlands: International Ballistics Society, 1983, vol. 21, p. 541–547.

[14] Johnson, G. R. and Cook, W. H. Fracture characteristics of three metals subjected to various strains, strain rates, temperatures and pressures. *Engineering Fracture Mechanics*. 1985, vol. 21, no. 1, p. 31–48. DOI: 10.1016/0013-7944(85)90052-9. ISSN 0013-7944.

[15] La Rosa, G., Mirone, G. and Risitano, A. Post-necking elastoplastic characterization: degree of approximation in the Bridgman method and properties of the flow-stress/true-stress ratio. *Metallurgical and Materials Transactions A*. 2003, vol. 34, no. 3, p. 615–624. DOI: 10.1007/s11661-003-0096-y. ISSN 1073-5623.

[16] Ma, Y., Yang, H., Yang, X., Li, M. and Jia, B. *Research on Mechanisms of Crack Initiation of Rear Axle for a Passenger Car During Accelerated Life Testing in a Proving Ground*. 2025. Preprint. Available from: `https://doi.org/10.20944/preprints202504.0970.v1`.

[17] Mirone, G. A new model for the elastoplastic characterization and the stress–strain determination on the necking section of a tensile specimen. *International Journal of Solids and Structures*. 2004, vol. 41, no. 13, p. 3545–3564. DOI: 10.1016/j.ijsolstr.2004.02.011. ISSN 0020-7683.

[18] Palla, S. *Types of Suspensions*. Online. 2025. Available from: `https://www.spinny.com/blog/types-of-suspensions/`. [Cited 19. October 2025].

[19] Petruška, J. *MKP v inženýrských výpočtech*. Online. Brno: Brno University of Technology, Faculty of Mechanical Engineering, 2011. Course notes. Available from: `http://www.umt.fme.vutbr.cz/images/opory/MKP%20v%20inzenyrskych%20vypoctech/RIV.pdf`. [Cited 16. October 2025].

[20] Sabhadiya, J. *MacPherson Struts vs. Double Wishbone Suspension*. Online. 2025. Available from: `https://www.mendmotor.com/macpherson-struts-vs-double-wishbone-suspension/`. [Cited 12. November 2025].

[21] Schulz, J. C. Finite element hourglassing control. *International Journal for Numerical Methods in Engineering*. 1985, vol. 21, No. 6, p. 1039–1048. DOI: 10.1002/nme.1620210607. ISSN 0029-5981.

# LIST OF FIGURES

2.1 The main components of a suspension system [4] . . . 23
2.2 The solid axle suspension with leaf springs [9] . . . 24
2.3 The torsion beam suspension with highlighted parts [6] . . . 25
2.4 Comparison between the MacPherson strut and the double wishbone suspension [20] . . . 26
2.5 Multilink suspension with highlighted control arms [6] . . . 26
3.1 Deformed geometry with a pronounced hourglass effect . . . 31
4.1 Geometry of analyzed rear torsion beam axle with dimensions in mm . . . 35
4.2 Comparison between the original solid geometry and the resulting surface geometry of the rear torsion beam axle . . . 36
4.3 Models of all used obstacles . . . 36
4.4 Geometry of all used obstacles . . . 37
4.5 Placement of the obstacle from the top view . . . 38
4.6 Comparison between two vertical placements of the obstacle . . . 38
4.7 Finite element mesh of used torsion beam axle . . . 39
4.8 Finite element mesh of all selected obstacles . . . 40
4.9 Placement of the spring and the shock absorber . . . 41
4.10 Defined nonlinear curves for the spring and the damper . . . 42
4.11 Model of used torsion beam suspension with detailed view of the wheel mount . . . 43
4.12 Model of boundary conditions with highlighted directions of unconstrained degrees of freedom at specific locations . . . 45
4.13 Geometry of the smooth specimen used for experimental tensile test . . . 48
4.14 Finite element mesh and boundary conditions used in the tensile test simulation of the smooth specimen . . . 48
4.15 Comparison of force reaction–displacement dependencies for the smooth specimen . . . 49
4.16 Multilinear equivalent stress–equivalent plastic strain curve approximated by Johnson–Cook power law function . . . 50
4.17 Comparison of reaction force–displacement dependencies of quasi-static and dynamic tests . . . 50
4.18 Geometry of the notched specimen used for experimental tensile test . . . 51

4.19 Finite element mesh and boundary conditions used in the tensile test simulation of the notched specimen . . . 52

4.20 Comparison of reaction force–displacement dependencies for the notched specimen . . . 52

4.21 Dependencies of fracture strain on stress triaxiality approximated by Johnson–Cook failure model function . . . 54

4.22 Dependency of stress triaxiality on equivalent plastic strain for dynamic test (right side) obtained from calibrated numerical model (left side) . . . 55

4.23 Dependencies used is the tabulated Johnson–Cook material model . . . 56

5.1 Resultant contact force (`RCFORCE`) comparison for analyzed obstacle geometries at 50 km/h . . . 59

5.2 Comparison of vehicle velocity reduction during impact for all modeled obstacle geometries . . . 60

5.3 Distribution of the damage parameter after impact at 50 km/h for all modeled obstacle geometries . . . 61

5.4 Distribution of the damage parameter after impact to the triangular obstacle at all initial velocity magnitudes . . . 62

5.5 Comparison of average relative velocity reduction across the analyzed velocity range for all simulated scenarios . . . 63

5.6 Comparison of a damage parameter distribution at different vertical position of the obstacle for initial velocity of 50 km/h . . . 64

5.7 Comparison of the reaction force for both vertical positions for all obstacle geometries at 50 km/h . . . 65

5.8 Hardening curve comparison between the calibrated and tabulated Johnson–Cook model and the Johnson–Cook model from [1] . . . 67

5.9 Reaction force comparison between the calibrated and tabulated Johnson–Cook model and the Johnson–Cook model from [1] . . . 68

5.10 Comparison of internal energy dissipation between the calibrated Tabulated Johnson–Cook model and the Johnson–Cook model from [1] . . . 69

5.11 Comparison of equivalent plastic strain distributions for both studied material models . . . 69

5.12 Experimental setup for the dynamic impact validation . . . 70

5.13 Geometry and finite element discretization of the experimental impactor . . . 71

5.14 Comparisons of velocity reduction curves (on the left) and reaction force profiles between experimental and numerical results . . . 72

5.15 Comparison of deformed geometries after the impact between experimental and numerical results . . . 72

# LIST OF TABLES

4.1 Defined termination times for varying initial velocity magnitudes . . . . . 45
4.2 Calibrated material parameters for the Johnson–Cook plasticity model . . 49
4.3 Values of average stress triaxiality and fracture strain obtained from numerical simulations . . . . . 53
4.4 Calibrated coefficients of Johnson–Cook failure model . . . . . 55
4.5 Input parameters for the tabulated Johnson–Cook material model . . . . . 57
5.1 Comparison of crack initiation in all simulated impact scenarios . . . . . 66
5.2 Input parameters for the Ahmad Johnson–Cook material model [1] . . . . 67

# A APPENDIX

### Listing of all used LS-DYNA Keywords

This appendix includes all used LS-DYNA keywords in creating of computational model with a settings example. A full explanation of all keywords used is available in LS-DYNA manuals [2, 3].

All physical values are provided in the **[t, mm, s, N]** unit system.

1. **Boundary conditions**

```
*BOUNDARY_PRESCRIBED_MOTION_RIGID
$      sid       dof       vad      lcid        sf       vid     death     birth
$#     pid       dof       vad      lcid        sf       vid     death     birth
        18         2         2        28       1.0         0       0.0       0.0

*BOUNDARY_SPC_SET
$     nsid       cid      dofx      dofy      dofz     dofrx     dofry     dofrz
$#    nsid       cid      dofx      dofy      dofz     dofrx     dofry     dofrz
        89         0         1         1         1         1         1         1
```

2. **Constraints**

```
*CONSTRAINED_EXTRA_NODES_NODE
$#     pid       nid     iflag
        18    156258         0
        18    156259         0
        11    156262         0
        11    156263         0
        17    156261         0
        17    156260         0
         6    156264         0
         6    156265         0

*CONSTRAINED_NODAL_RIGID_BODY
$      pid       cid      nsid     pnode      iprt    drflag    rrflag
$#     pid       cid      nsid     pnode      iprt    drflag    rrflag
        23         0         5         0         0         0         0

*CONSTRAINED_RIGID_BODIES
$#    pidl      pidc     iflag
        18        15         0
        17        16         0

*CONSTRAINED_JOINT_REVOLUTE_ID
2
156261    156264    156260    156265         0         0       1.0       1.0
```

## 3. Contacts

```
*CONTACT_TIED_NODES_TO_SURFACE_OFFSET_ID
$#     cid                                                                title
287Bonded - Midsurface - Result of Solid_ACHSLENKER_LI_finished2\Midsurfa
$      ssid      msid     sstyp     mstyp    sboxid    mboxid       spr       mpr
$#    surfa     surfb  surfatyp  surfbtyp   saboxid   sbboxid      sapr      sbpr
         15        16         4         0         0         0         1         1
$        fs        fd        dc        vc       vdc    penchk        bt        dt
$#       fs        fd        dc        vc       vdc    penchk        bt        dt
        0.0       0.0       0.0       0.0      10.0         0       0.0       0.0
$       sfs       sfm       sst       mst      sfst      sfmt       fsf       vsf
$#     sfsa      sfsb      sast      sbst     sfsat     sfsbt       fsf       vsf
        0.0       0.0       0.0       0.0       0.0       0.0       0.0       0.0
$      soft   softscl    lcidab    maxpar     sbopt     depth     bsort   frcfrq
$#     soft    sofscl    lcidab    maxpar     sbopt     depth     bsort   frcfrq
          0       0.0         0       0.0         3         5         0         0
$    penmax    tkhopt    shlthk     snlog      isym     i2d3d    sldthk   sldstf
$#   penmax    thkopt    shlthk     snlog      isym     i2d3d    sldthk   sldstf
        0.0         0         0         0         0         0       0.0       0.0

*CONTACT_AUTOMATIC_SURFACE_TO_SURFACE_ID
$#     cid                                                                title
403axle/obstacle
$#    surfa     surfb  surfatyp  surfbtyp   saboxid   sbboxid      sapr      sbpr
         1        14         3         3         0         0         0         0
$#       fs        fd        dc        vc       vdc    penchk        bt        dt
        0.3       0.2      0.01       0.0      20.0         0      0.01.00000E20
$#     sfsa      sfsb      sast      sbst     sfsat     sfsbt       fsf       vsf
        1.0       1.0       0.0       0.0       1.0       1.0       1.0       1.0
```

## 4. Controls

```
*CONTROL_TERMINATION
$#  endtim    endcyc     dtmin    endeng    endmas      nosol
      0.03  10000000     0.001       0.0  100000.0          0
```

## 5. Hourglass

```
*HOURGLASS_TITLE
shell
$#     hgid       ihq        qm       ibq        q1        q2    qb/vdc        qw
          1         4       0.1         0       1.5      0.06       0.1       0.1
```

## 6. Initial conditions

```
*INITIAL_VELOCITY_GENERATION
$       sid      styp     omega        vx        vy        vz     ivatn      icid
$#       id      styp     omega        vx        vy        vz     ivatn      icid
          9         2       0.0  -13890.0       0.0       0.0         0        63
$#       xc        yc        zc        nx        ny        nz     phase    irigid
        0.0       0.0       0.0       0.0       0.0       0.0         0         0

*INITIAL_VELOCITY_RIGID_BODY
$       pid        vx        vy        vz       vxr       vyr       vzr      icid
$#      pid        vx        vy        vz       vxr       vyr       vzr      icid
         30  -13890.0       0.0       0.0       0.0       0.0       0.0        63
```

## 7. Loads

```
*LOAD_BODY_Z
$     lcid        sf    lciddr        xc        yc        zc       cid   unused1
$#    lcid        sf    lciddr        xc        yc        zc       cid
          4       1.0         0       0.0       0.0       0.0        63
```

# 8. Material models

```
*MAT_ELASTIC
$       ID         ro          E        pr        da        db         k   unused1
$#     mid         ro          e        pr        da        db  not used  not used
   2 7.85000E-9   210000.0      0.33       0.0       0.0         0         0

*MAT_RIGID
$       ID         ro          E        pr         n    couple         m     alias
$#     mid         ro          e        pr         n    couple         m     alias
        15 3.26000E-5 5.00000E-6       0.3       0.0       0.0      0.00

*MAT_TABULATED_JOHNSON_COOK_TITLE
TabulatedJC
$#     mid         ro          e        pr        cp        tr      beta    numint
        37 7.85000E-9   229600.0       0.3       1.0      24.0       1.0       3.0
$#    lck1       lckt        lcf       lcg       lch       lci     bflgi
        39          0         40        41         0        44         0

*MAT_SPRING_NONLINEAR_ELASTIC_TITLE
nonlinear_spring
$#     mid        lcd        lcr
        39         42          0

*MAT_DAMPER_NONLINEAR_VISCOUS_TITLE
damper_nonlinear
$#     mid       lcdr
        40         43
```